Science of the Total Environment 777 (2021) 144579

Contents lists available at ScienceDirect

Science of the Total Environment

journal homepage: www.elsevier.com/locate/scitotenv

Understanding the local and remote source contributions to ambient O_3 during a pollution episode using a combination of experimental approaches in the Guadalquivir valley, southern Spain

M. in 't Veld [a,b,*], C. Carnerero [a,b], J. Massagué [a,c], A. Alastuey [a], J.D. de la Rosa [d], A.M. Sánchez de la Campa [d], M. Escudero [e], E. Mantilla [f], G. Gangoiti [g], C. Pérez García-Pando [h,i], M. Olid [h], J.R. Moreta [j], J.L. Hernández [j], J. Santamaría [j], M. Millán [f], X. Querol [a]

[a] Institute of Environmental Assessment and Water Research, IDAEA-CSIC, Barcelona 08034, Spain
[b] Department of Civil and Environmental Engineering, Universitat Politècnica de Catalunya (UPC), Barcelona 08034, Spain
[c] Department of Mining, Industrial and ICT Engineering, Universitat Politècnica de Catalunya (UPC), Manresa, 08242, Spain
[d] Department of Geology, University of Huelva, Huelva 21819, Spain
[e] Centro Universitario de la Defensa, Academia General Militar, Zaragoza 50090, Spain
[f] Centro de Estudios Ambientales del Mediterráneo, CEAM, Valencia 46980, Spain
[g] Department of Chemical and Environmental Engineering, University of Basque Country, Leioa 48940, Spain
[h] Barcelona Supercomputing Center, BSC-CNS, Barcelona 08034, Spain
[i] Catalan Institution for Research and Advanced Studies, ICREA, Barcelona 08010, Spain
[j] Agencia Estatal de Meteorología, AEMET, Madrid 28071, Spain

HIGHLIGHTS

- A complex orographic-meteorological scenario accommodated regional O_3 accumulation.
- The O_3 accumulation increased O_3 with 25–30 ppb due to the recirculating air masses.
- On top of this, local contributions increased O_3 levels up to 20 ppb.
- Abundant agricultural burning increased O_3 with 10 ppb later on the day.
- Source-tracing pollutants were used to associate O_3 peaks to specific sources.

GRAPHICAL ABSTRACT

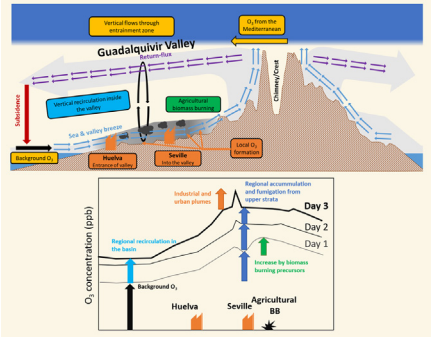

ARTICLE INFO

Article history:
Received 17 August 2020
Received in revised form 10 December 2020
Accepted 13 December 2020
Available online 20 February 2021

Editor: Lidia Morawska

Keywords:
Regional atmospheric pollution
Photochemistry
Agricultural burns
Ozone meteorology

ABSTRACT

The Guadalquivir Valley is one of three major O_3 hotspots in Spain. An airborne and surface measurement campaign was carried out from July 9th to 11th, 2019 to quantify the local/regional O_3 contributions using experimental approaches. Air quality and meteorology data from surface measurements, a microlight aircraft, a helium balloon, and remote sensing data (TROPOMI-NO2-ESA) were used to obtain the 3D distribution of O_3 and various tracer pollutants.

O_3 accumulation over 2.5 days started with inputs from oceanic air masses transported inland by sea breezes, which drew O_3 and its precursors from a local/regional origin to the northeastern end of the basin. The orographic–meteorological setting of the valley caused vertical recirculation of the air masses inside the valley that caused the accumulation by increasing regional background O_3 concentration by 25–30 ppb. Furthermore, possible Mediterranean O_3 contributions and additional vertical recirculation through the entrainment zone of the convective boundary layer also contributed. Using particulate matter finer than 2.5 μm ($PM_{2.5}$), ultrafine particles (UFP), and black carbon (BC) as tracers of local sources, we calculated that local contributions increased

* Corresponding author at: Institute of Environmental Assessment and Water Research, IDAEA-CSIC, Barcelona 08034, Spain.
E-mail address: marten.veld@idaea.csic.es (M. in 't Veld).

https://doi.org/10.1016/j.scitotenv.2020.144579

regional O_3 levels by 20 ppb inside specific pollution plumes transported by the breeze into the valley, and by 10 ppb during midday when flying over an area with abundant agricultural burning during the morning. Air masses that crossed the southern boundaries of the Betic system at mid-altitude (400–1850 m a.s.l.) on July 10th and 11th may have provided additional O_3. Meanwhile, a decreasing trend at high altitudes (3000–5000 m a.s.l.) was observed, signifying that the impact of stratospheric O_3 intrusion decreased during the campaign.

1. Introduction

Tropospheric ozone (O_3) is a secondary gaseous pollutant involved with complex chemical processes that affects human health, ecosystems, and climate (Monks et al., 2014, 2015). Its photochemical production, involving the oxidation of non-methane volatile organic compounds (non-methane VOCs), methane (CH_4), and carbon monoxide (CO), with the latter two being more relevant for hemispheric transport of O_3 (Jacob, 1999a, 1999b), accounts for approximately 90% of global tropospheric O_3. Photochemical oxidation produces oxidizing radicals that oxidize nitrogen oxide (NO) into nitrogen dioxide (NO_2). The NO_2 will then subsequently generate activated oxygen (O^*) by photolysis ($NO_2 = NO + O^*$), which reacts with molecular oxygen (O_2) to generate O_3. The remaining ~10% of O_3 originates from stratospheric intrusions (Greenslade et al., 2017; Stevenson et al., 2006; Young et al., 2013).

Tropospheric O_3 has negative effects on human health, natural vegetation, and crops due to its highly oxidizing nature. It can have acute and chronic effects on pulmonary and cardiovascular morbidity, and can even cause premature mortality (Amann et al., 2008; Lelieveld et al., 2017, 2020). It is therefore considered one of the most harmful air pollutants in the troposphere together with particulate matter (PM) and NO_2 (HEI, 2018; WHO, 2016). In 2005, the WHO Air Quality Guidelines (WHOAQG) established a recommended maximum O_3 concentration of 100 μg/m^3 over an 8-hour period moving average throughout the day (WHO, 2006). This recommendation was not copied by the European Union, which set the limit at 120 μg/m^3 over an 8-hour average, with the added condition that the limit cannot be exceeded more than 25 times/year averaged over a three-year period (2008/50/CE) (European Parliament and Council of the European Union, 2008). Additionally, the European standards establish information and alert thresholds at hourly concentrations of 180 and 240 μg/m^3, respectively (European Parliament and Council of the European Union, 2008). According to the European Environmental Agency (EEA), between 2013 and 2015 more than 95% of the urban population in EU-28 was exposed to O_3 levels exceeding the WHOAQG (EEA, 2018). These exceedances are much more frequent and intense in Southern Europe, where the climate and specific meteorological and orographic patterns, along with intensive emissions of anthropogenic and biogenic precursor emissions, favor O_3 formation (Millán et al., 1997, 2002; Millán, 2014; among others).

In recent decades, EU emission abatement policies have had general success in reducing both mean and peak ambient air concentrations of primary PM, VOCs, sulfur dioxide (SO_2), and NO_x ($NO_2 + NO$). However, the ambient concentrations of secondary pollutants, such as O_3, did not follow a similar trend (Table S2) (Colette et al., 2016; EEA, 2018, 2019; Paoletti et al., 2014; Querol et al., 2014, 2016). In Europe, from 2003 to 2012, the annual mean O_3 concentrations increased by 4.1% overall and by 17% in urban areas (Colette et al., 2016; EEA, 2018, 2019), while the frequency and intensity of high O_3 episodes decreased by 12% (Colette et al., 2016). The increasing urban O_3 concentrations have been attributed to the decrease of NO_x in VOC-dominated environments, and/or to the reduction of NO/NO_2 ratios, which reduces the capacity of the troposphere to titrate O_3 ($NO + O_3 = NO_2 + O_2$) (Escudero et al., 2014; Massagué et al., 2019; Querol et al., 2016). In Spain, Querol et al. (2016) identified the reduction of NO/NO_2 ratios, with a 50–62% decrease in NO concentrations compared to a 31–34% decrease in NO_2 concentrations between 2000 and 2015. This resulted in a decreased O_3 titration potential, which in turn was identified as the major cause of increasing urban O_3 levels (Jhun et al., 2015; Querol et al., 2016). Reducing the tropospheric O_3 concentration is quite challenging due to the complex nature of the atmospheric and chemical processes governing its formation:

(I) O_3 has a wide variety of precursors (Bergin et al., 1998; Carter, 2000, 2009; Carter et al., 1999).
(II) O_3 and some of its precursors have long residence times in the atmosphere, facilitating long-range transport (Dentener et al., 2010).
(III) O_3 can accumulate in atmospheric basins under certain atmospheric conditions, due to the combination of topography and specific meteorological patterns (Gangoiti et al., 2001; Millán, 2014; Millán et al., 1997, 2002).
(IV) The reactions of VOCs and NO_x are non-linear (Monks et al., 2015, and references therein).
(V) O_3 intrusions can occur from the stratosphere as well as tropospheric influence (Kalabokas et al., 2017).

Reducing the ambient O_3 levels is especially challenging in areas of Southern Europe, such as Spain, that are vulnerable due to low precipitation, high insolation, high NO_2 pollution, high biogenic VOC emissions, and vertical recirculation of air masses due to orographic features and meteorological patterns (Gangoiti et al., 2001; Millán, 2014; Millán et al., 1997, 2002; Pérez et al., 2004; Querol et al., 2017). Dieguez et al. (2009, 2014) and Querol et al. (2016) identified several atmospheric basins in the northeastern, central, eastern, and southern regions of the Iberian Peninsula, which recorded the most frequent and intense O_3 pollution episodes.

Our study focuses on one of these basins, the Guadalquivir Valley (GV), which crosses the southern Iberian Peninsula in a northeastern–southwestern direction (Fig. 1). Prior studies of O_3 in the GV (Castell et al., 2009, 2011; Dieguez et al., 2009, 2014; INTA, 2006a) found two urban air quality monitoring stations (hereafter AQMS) with persistently very high O_3 concentrations in Córdoba, a city located deep in the valley, suggesting a significant contribution from regional transport; eight stations in the metropolitan area of Seville showed lower O_3 concentrations on weekends. The maximum concentrations of O_3 during midday and in the early afternoon were hypothesized to have a double origin. First, O_3 is formed and transported from the coastal areas of Huelva and Cádiz; second, O_3 comes from the recirculated pollution plumes of the city of Seville that originated in previous days. Also, the areas potentially affected most by the pollution plume of Seville were found to be located to the northeast of the city (Adame et al., 2008; INTA, 2006b; Pay et al., 2019). In analyzing the entire Andalusian region, these studies found that the 2000–2008 exceedances of the hourly information threshold (tracing the most polluted O_3 episodes) occurred mostly in the western GV (up to 5.3 exceedances per year in Seville). There were neither clear interannual trends nor apparent influences of the average and maximum daily temperatures; the major driver of the exceedances was found to be the number of breezy days.

Adame et al. (2009) studied four stations in Huelva, located at the western end of the GV, and found three important trends. First, southwesterly winds were common during sea breeze circulation in the

Fig. 1. Study area of the campaign and the location of the air quality stations used (blue), cities and their most noteworthy emission sources (red), the location of the O_3 sounding (yellow), and the flight path (purple line) of the plane measurements and its starting point (purple star). (For interpretation of the references to colour in this figure legend, the reader is referred to the web version of this article.)

summer. Second, the average monthly concentrations were at a maximum of 96–72 μg/m^3 in June and July, compared to 62–40 μg/m^3 during January and December. Finally, exceedances of the thresholds were frequent, especially at one station located on the coast. Dieguez et al. (2009) attributed the high O_3 concentrations in Seville, which is one of the largest cities in Spain, to the interaction of urban traffic, NO_x emissions, and VOCs transported by sea breezes from the petrochemical emissions of Huelva. They also noted that when urban plumes are transported, a shift occurs from the usual condition of VOCs-limited O_3 formation to NO_x-limited conditions.

Pay et al. (2019) studied the sources of O_3 in Spain, which included an urban station in Seville and one rural station near the coast. They concluded that the GV had one of the highest daily O_3 concentrations in Spain, with the largest source of anthropogenic O_3 (approximately 18%) originating from the on-road traffic from Seville, Huelva, and Cordoba; followed by shipping (approximately 17%).

These prior studies were based on air quality data interpretation, but none focused on combining these with airborne measurements during high O_3 episodes to devise a conceptual model for the occurrences and causes of these episodes. In this context, we aim to understand O_3 episodes in the GV, focusing on the Seville metropolitan area, where the most intense O_3 episodes were recorded. To this end, a campaign of land-based and airborne measurements was carried out in the second week of July 2019, when the probability of a high O_3 episode was the highest. This work will provide insight into the phenomenology of O_3 formation in this area, and gives us the ability to quantify the contributions of local and regional sources of O_3 using experimental approaches. We used black carbon (BC), PM finer than 2.5 μm ($PM_{2.5}$), and ultrafine particles (UFP; particles of less than 100 nm in diameter) as tracers of different regional/local sources influencing O_3 formation.

2. Methodology

To investigate the phenomenology of high O_3 episodes in the GV, an intensive land-based and airborne O_3, $PM_{2.5}$, BC, and UFP measurement campaign was performed between July 9th and 11th, 2019. The dates of the campaign were selected based on an analysis of an O_3 time series of 24 AQMSs (Table S3) in the GV between 2005 and 2018, which showed the 190th–200th days of the year to be the period with the maximum number of days exceeding an arbitrary hourly O_3 threshold of 150 μg/m^3, which occurred mostly around Seville City (in particular, at the Aljarafe AQMS). The campaign was carried out during working days to avoid the typical weekend O_3 drop shown by the data.

The 3D spatial and temporal variability of O_3 concentrations, along with those of other pollutants, and meteorological parameters were measured using airborne instrumentation. Nine free O_3 soundings launched from Mairena del Aljarafe (Fig. 1, yellow star) provided vertically-resolved measurements of O_3 and meteorological parameters. An instrumented microlight plane was used simultaneously to characterize the horizontal variability of O_3, $PM_{2.5}$, BC, UFP, temperature, and relative humidity (RH) across the nine flights covering 250 km each.

These tailored measurements were complemented with surface O_3 concentration measurements from the AQMSs located in the GV from Huelva, in the west, to Jaén, in the east (Fig. 1); meteorological data from the Spanish Meteorological Office (AEMET); NO_2 data from the Tropospheric Monitoring Instrument of the European Space Agency (TROPOMI-ESA) satellite measurements; high-resolution outputs from the operational air quality forecast system of Spain (Spanish: CALIdad del aire Operacional Para España: CALIOPE); the mesoscale Regional Atmospheric Modeling System/HYbrid PArticle Concentration and Transport (RAMS/HYPACT) modeling system; and the Hybrid Single-Particle Lagrangian Integrated Trajectory (HYSPLIT) trajectory model.

2.1. Study area

The GV is located in the southern part of the Iberian Peninsula (Fig. 1), crossing nearly the entire Andalusian territory for 650 km in a northeastern–southwestern direction. In addition to the Guadalquivir River that flows into the GV, the Odiel and Tinto rivers also have estuaries on the Atlantic coast. From its beginning in the Sierra de Cazorla, the GV becomes progressively wider towards the Atlantic Ocean, occupying an approximate area of 57000 km^2 with widths of more than 150 km. In this paper, altitudes are written in meters above sea level (m a.s.l.), but the elevation of the valley increases from sea level at the Atlantic Ocean coast towards the Sierra de Cazorla. A cross-section of the valley is shown in Fig. S1. At its western end, the Guadalquivir lies at sea level (0 m a.s.l.) at the Atlantic Ocean, near Huelva. Eastward from the coast, the elevation increases to about 200 m a.s.l. at 200 km into the valley. Further eastward, the elevation increases more rapidly towards the mountain ranges of Sierra Mágina and Sierra de Cazorla, to higher than 1000 m a.s.l. Two large mountainous systems surround the GV: the Sierra Morena in the north, which acts as a natural border with the Central Plateau; and the Betic System to the south. Geographical factors of the area, such as the orography and topography, establish some continental climatic regionalization within the dominant Mediterranean climate, with high temperatures, irregular precipitation, and intense heatwaves (Adame et al., 2009; Dieguez et al., 2009). The wide opening of the GV at the Atlantic Ocean has no significant orographic barriers, which favors a relatively humid climate on the coast. Farther into the valley, the wet Atlantic influence weakens, and the continental features increase, bringing less rainfall and more aridity, especially in the upper part of the valley. Intense sea breezes develop quite frequently inside the GV, especially in July, due to the very high inland temperatures (36 °C and 20.3 °C are the annual average daily maximum and minimum temperatures, respectively, in Seville in July) in contrast with the cooler Atlantic air masses (data accessed from AEMET[1]).

The most relevant emission sources in the area are (Fig. 1):

(I) Traffic emissions from the cities of Seville (703,200 inhabitants), Córdoba (328,400 inhabitants), Huelva (148,800 inhabitants), Cádiz (126,800 inhabitants),[2] and Jaén (116,500 inhabitants); numerous smaller conurbations; and highly trafficked highways.
(II) Industrial emissions from the large industrial estates of Huelva, which includes one of the largest petrochemical estates in Spain; fertilizer plants; a large copper smelter; and a large industrial harbor, among others, as well as industries of other cities.
(III) Thermal power plants of Arcos (near Cádiz), Huelva, Cádiz, and Córdoba.
(IV) Seville airport.
(V) The dense maritime transport in the Strait of Gibraltar.
(VI) Agricultural, farming, and food industry emissions, which include intense biomass burning throughout the valley and the oil production plants in its central and upper parts.

Apart from these anthropogenic sources of O_3 precursors, there are also significant sources of biogenic VOC precursors in the area, such as large forested areas, crop plantations (citrus and olive groves in the central and upper areas, and fruit trees, including citrus, in the lower areas), and estuarine marshes.

2.2. Surface air quality data, modeling, and satellite data

In order to support interpretations of the airborne measurements carried out during the campaign, we used ground-level measurement data from 55 AQMSs of the Andalusian Regional Government and four AQMSs from the European Monitoring and Evaluation Programme (EMEP) monitoring network, run in this case by AEMET (Table S4). These stations are equipped with instrumentation to measure concentrations of O_3, NO_x, SO_2, PM_{10}, and $PM_{2.5}$. Furthermore, we used O_3 concentration maps for the Iberian Peninsula from the CALIOPE air quality forecast system at 4 × 4 km resolution (Baldasano et al., 2008, 2011). Tropospheric NO_2 background levels with a resolution of 7.2 × 3.6 km were obtained from the Tropospheric Monitoring Instrument (TROPOMI) installed onboard the Sentinel-5 Precursor (SP-5) satellite of the European Space Agency (ESA) (Veefkind et al., 2012).

Mesoscale meteorological fields and backward–forward trajectories of tracer particles were generated with the RAMS v6.0 (Pielke et al., 1992) and HYPACT v1.5 models (Tremback et al., 1994), respectively, to interpret the origin of the O_3- enriched free tropospheric layers (Section 3.3) and the contributions of regional background O_3/precursors to the mixing layer along the GV. Three domain grids with increasing resolutions of 48, 12, and 3 km were used following a deployment similar to that in Pey et al. (2008). Similarly, in the vertical direction, 44 levels with variable resolution (30 m at ground level and 1000 m

[1] http://www.aemet.es/es/serviciosclimaticos/datosclimatologicos/valoresclimatologicos?l=5783&k=41
[2] https://worldpopulationreview.com/countries/cities/spain

in the upper troposphere) were used for all the grids, with a total coverage of 22,400 m. The horizontal boundaries of the largest domain, covering the Iberian Peninsula, Southern Europe, and Northern Africa, were adjusted to the conditions given by the European Centre for Medium-Range Weather Forecasts (ECMWF) ERA-Interim reanalysis (Dee et al., 2011) at 00:00, 06:00, 12:00, and 18:00 UTC (0.75° × 0.75° latitude–longitude grid resolution).[3] Four-dimensional data assimilation by nudging was used for the RAMS–HYPACT model run, with Newtonian relaxation around the six-hourly ERA-Interim data. A variable relaxation time was used, with the highest values (weak nudging) at the center of the parent domain, and the lowest values (strong nudging) at the boundaries. Topography and land cover were interpolated from the USGS global 30″ database[4,5] (Gesch et al., 1999) . Daily sea surface temperature (SST) data, with an original resolution of 0.25° × 0.25°, were interpolated for this simulation from the Optimum Interpolation SST (OISST) Advanced Microwave Scanning Radiometer with Advanced Very High Resolution Radiometer (AMSR-AVHRR) analysis[6] (Banzon et al., 2016; Reynolds et al., 2007) into the model grids. Our setup of the mesoscale model included a prognostic turbulent kinetic energy (level 2.5) parameterization (Mellor and Yamada, 1982), with modifications for the case of growing turbulence (Helfand and Labraga, 1988), and a full-column two-stream parameterization that accounted for each form of condensate (seven species) for the calculations of the radiative transfer through clouds and gases in the model (Harrington et al., 1999). The RAMS run from 00:00 UTC on July 4th to 00:00 UTC on July 12th was performed continuously. Hourly meteorological fields estimated by RAMS were forwarded to the HYPACT model to perform the dispersion evaluation of the atmospheric passive tracer.

For the forward trajectories, a total of 17 city-sources of vertical emission lines (0–300 m in height) were selected using a scheme similar to that in Pey et al. (2008). The variable height of the particle release, from the surface to 300 m a.g.l., accounts for a wide variety of effective emission heights in urban and industrial environments. The selection of coastal Mediterranean, Atlantic, and inland city-sources encompassed an area of diverse weather and wind regimes. This methodology allowed us to simulate different transport mechanisms operating in the area. The sources were grouped into five areas as follows: North-Atlantic (Nantes, Bilbao, La Coruña, Lisbon, Porto), South-Atlantic (Huelva, Seville, Cádiz), North-Mediterranean (Marseille, Barcelona, Tarragona), South-Mediterranean (Valencia, Cartagena, Malaga), and Iberian-inland (Madrid, Valladolid, Zaragoza). Particle releases started on July 4th and lasted eight days, and the 3D positions of 38400 particles for each of the 17 city-source simulations were tracked for the whole period until July 12th.

In order to support the interpretations of the airborne measurements along the GV, the dynamics of urban plumes and industrial plumes of the Huelva petrochemical plant were modeled using the HYSPLIT model (Draxler and Hess, 1998; Stein et al., 2015) of the National Oceanic and Atmospheric Administration (NOAA). Specifically, behavior was modeled for emissions derived from two plume sources: the CEPSA La Rábida Refinery, located in the industrial area of Huelva (geographical coordinates WGS84: 37.2°N, 6.9°W, altitude 140 m a.s.l.); and traffic emissions in a 1 km^2 area of Seville (geographical coordinates WGS84: 37.4°N, 6.0°W, altitude 10 m a.s.l.) The HYSPLIT model was run through the METEOSIM platform.[7] In the simulations, the meteorological domain used a resolution of 3 km, with data obtained from the Global Data Assimilation System (GDAS) and using a common emission rate of 100 g/s for $PM_{2.5}$. The duration of the simulation was 12 h, and the distribution of the plume was obtained every hour during the period of the campaign.

2.3. O_3 soundings

Vertical variations in O_3 concentration and meteorological parameters were measured with nine free O_3 soundings, launched every day between July 9th–11th, 2019, at 06:00, 12:00, and 17:00 (UTC), from the El Olivo school 37.3°N, 6.0°W, at 58 m a.s.l., very close to the Aljarafe AQMS, 10 km south of Seville and 25 km from the Guillena airfield (Fig. 1). The instrumentation launched consisted of an RS41-SGP (Vaisala) radiosonde combined with an EC3-6A O_3 sensor (Science Pump Corporation) attached to a helium balloon. The partial pressure of O_3, T, RH, GPS location, wind speed, and wind direction were measured at a frequency of 1 s up to an altitude of approximately 30 km, which was reached approximately 2 h after each launch.

2.4. Microlight measurements

The horizontal variation of pollutant concentrations in the lower part of the atmosphere was measured using instrumentation onboard a microlight (single-engine Tecnam P96 Golf) that flew daily at 06:00, 11:30, and 17:30 UTC, with an approximate flight duration of 2 to 2.5 h per flight. The same route (Fig. 1) was repeated for each flight, at an altitude ranging between 150 and 550 m a.s.l.: departing from the Guillena airfield (37.6°N, 6.0°W), heading southbound towards Seville, then to the southwest towards Huelva, with a descent and subsequent ascent upon arrival at the Atlantic coast, a return towards the northeast over Guillena to Lora del Río, and then heading back to Guillena. The measurement devices (Table S5) were placed inside the cabin and connected to an inlet designed for high-speed particle measurement installed in the right front ventilation inlet (Fig. S2).

Black carbon concentrations were measured using a microAeth® aethalometer (Magee Scientific Corporation, 1 min resolution); $PM_{2.5}$ concentrations with a Dusttrak DRX aerosol monitor (TSI, 10 s resolution); UFP number concentration and average particle size in the 10–700 nm size range with a diffusion particle size classifier (N and D_p, respectively) (DiSCMini; Testo, 10 s resolution); and O_3 concentrations with a personal O_3 photochemistry monitor (POM; 2B Technologies, 10 s resolution). The instruments were connected with a Teflon© inlet pointing towards the rear of the aircraft to reduce air flow. In addition, a portable weather monitor for temperature and RH (Kestrel 4500) was installed on the exterior of the aircraft attached to the landing gear and pointing towards the front, and a GPS tracker was placed inside the plane, both with a time resolution of 10 s.

3. Results

3.1. Meteorological context and air mass tracking

The synoptic conditions during the three-day campaign were characterized by the Azores High located west of Iberia and its relative high-pressure area extending eastward, reaching both Southern Europe and the Western Mediterranean region (Fig. 2). Clear skies and surface low-pressure gradients under these anticyclonic conditions developed mesoscale circulations in the lower troposphere of the area. Land–sea breezes in the coastal areas flow inland while the mountain–valley winds give a compensatory flow. This circulation pattern governs the transport of O_3 in the lower troposphere of Southern Europe and the Western Mediterranean region, as was first reported by Millán et al. (1997) based on experimental evidence gathered during a series of intensive summer field campaigns in the region, and then by Gangoiti et al. (2001), among others.

The observed low-pressure gradient conditions at lower atmospheric levels contrasted with the rapid evolution at higher atmospheric levels. On July 9th, an upper-level low (marked #1 in Fig. 2b

[3] https://www.ecmwf.int/en/forecasts/datasets/
[4] https://www.usgs.gov/centers/eros/science/usgs-eros-archive-digital-elevation-global-30-arc-second-elevation-gtopo30
[5] https://www.usgs.gov/centers/eros/science/usgs-eros-archive-land-cover-products-global-land-cover-characterization-glcc
[6] https://www.ncdc.noaa.gov/oisst
[7] https://www.meteosim.com/es/

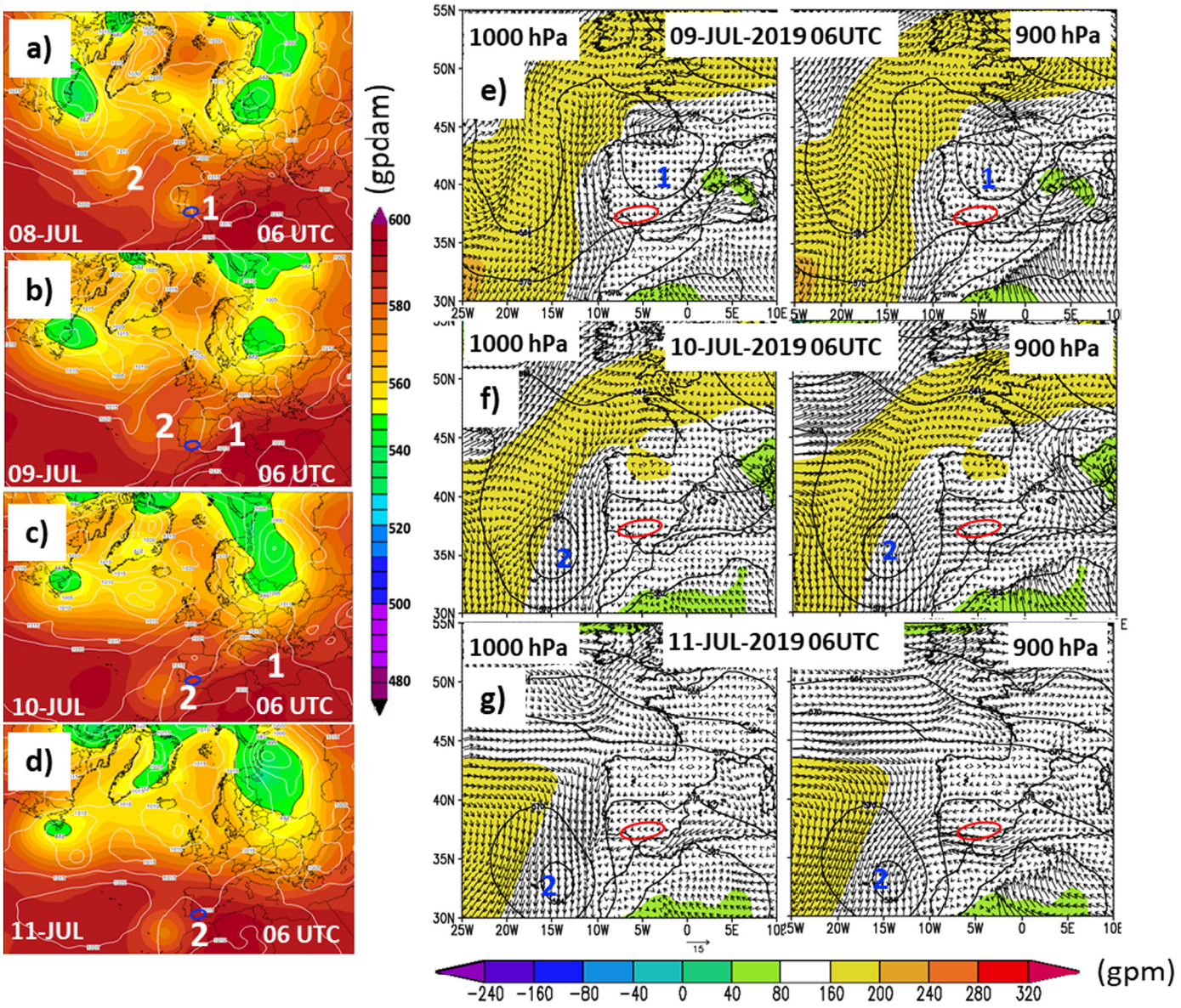

Fig. 2. Left: Climate Forecast System Reanalysis (CFSR): 500 hPa geopotential height (gpdams) and mean sea level pressure (MSLP) contours (hPa) at 06:00 UTC. during the period of July 8th (a), July 9th (b), July 10th (c), and July 11th (d), 2019 (Wetterzentrale, http://www.wetterzentrale.de; last access: March 31st, 2020. The blue circle indicates the study area. Right: ERA-Interim ECMWF reanalysis: winds at 1000 hPa and (right) at 900 hPa, represented with the geopotential height (gpm) of the 1000 hPa surface in shaded colors, and the 1000–500 hPa thickness (gpdams) in contours at 06:00 UTC during the period of the field campaign, July 9th (e), July 10th (f), and July 11th (g), 2019 (ECMWF, https://www.ecmwf.int/en/forecasts/datasets/; accessed 15th January 2020). The red area indicates the study area. (For interpretation of the references to colour in this figure legend, the reader is referred to the web version of this article.)

and e) crossed the Iberian Peninsula from southwest to northeast. This low had split from an upper-level trough over the North Atlantic six days before (not shown in the figure) and remained almost stationary during the following days over the west coast of Portugal (Fig. 2). The system brought deep convection and storms on July 8th, ahead of the low over the Iberian landmass. As the low-pressure system #1 moved into the Gulf of Lion and weakened on July 9th, more stable conditions developed over Iberia, with clear skies and northwesterlies (backing to the west in the free troposphere, above 2500–3000 m a.s.l. in the soundings discussed in Section 3.3). These conditions characterized cold advection at the rear of the upper-level low. The northwesterlies, associated with a deep dynamic sinking that affected almost the entire troposphere (Fig. S3, upper-right panel), were responsible for the transport of air masses enriched in O_3 from the middle and high troposphere (above 2500–3000 m a.s.l.) into the upper levels of the mesoscale circulations developed in the GV and recorded by the sounding in Seville on July 9th (Section 3.3). Also, based on the RAMS/HYPACT back-trajectories, we found the O_3 enriched layers at 3000–4000 m a.s.l. observed in Seville on July 9th to be associated with a tropopause folding following the evolution of the upper level low #1, as shown in Fig. S3b. None of the trajectories ending above 3000 m a.s.l. (3000–4000 m a.s.l.) at the sounding site in Seville between July 9th and 11th were found to be initiated at the boundary layer, after being tracked back to July 4th.

A second upper-level low (marked #2 in Fig. 2a) originated from another upper trough on July 8th in the North Atlantic and moved farther south than the upper low #1, reaching the western coast of Morocco on July 10th (Fig. 2c). This second low triggered important changes in the advection of air masses into the South-Atlantic region. It deepened on July 11th (Fig. 2d) and forced more intense southeasterly winds to veer towards the south and southwest in the free troposphere of the GV (warm advection), with a clear decrease in O_3 concentrations above 3000 m a.s.l., as recorded at the sounding site in Seville from July 10th to 11th (Section 3.3). However, these changes during the episode were not observed in the circulation at lower levels in the GV. The

monitoring stations recorded land–sea and mountain–valley breezes with locally developed circulations during the whole period.

In all, the origin of the background air masses incorporated into the basin changed completely from July 9th to July 11th. In the region of the Strait of Gibraltar (including the Gulf of Cadiz and the regions of the Alboran Sea to the west and east of the Strait), alternating easterly and westerly winds typically drive the local meteorology at low levels (Dorman et al., 1995). During the campaign, westerly winds associated with the cold advection on July 9th changed to easterly winds over the following two days (Fig. 2). At surface level (1000 hPa), these changes in the Strait started early on July 11th (following the onset of the mistral in the Gulf of Lion the day before), about 24 h later than at 900 hPa. In Sections 3.3 and 4, we discuss the accumulation of O_3 within the GV that occurred from July 9th to 11th, concurrent with the O_3 decreases in the free troposphere and the changes in the regional advection at lower layers. The sea breeze prevalence during the measurement campaign is supported by the wind speeds and directions measured at the State Meteorological Agency of Spain(AEMET) of Doñana-Almonte, Sevilla-Airport, and Bailén (from the coastal area to deep into the GV) reported in Fig. S4, with dominant daylight wind directions of around 250° and very high wind speeds, and light winds from inland with a 45° directional component. The vertical profiles that will be shown in subsequent sections also demonstrate the occurrence of a major sea breeze circulation during the measurement days. The changes in the background pollution inside the GV have been studied using RAMS/HYPACT forward trajectories for selected cities, as described in Section 2.2. Fig. S5 shows fumigation at low levels of the GV on July 9th of particle tracers released in the Atlantic sector (of the North Atlantic ocean), and the arrival of particle tracers originating in the Mediterranean to the east of the city of Malaga on July 10th and reaching the GV from the southeast, across the southern boundaries of the Betic System. This arrival of pollutants from the east occurred after the described changes in circulation from westerly to easterly 18 h before, which might have also included pollutants from other nearby coastal emissions, including road traffic, industries, and shipping. Interestingly, during the whole episode, most of the tracers were transported below a height of 3000–3200 m a.s.l., which was consistent with the existence of the recorded elevated temperature inversion at that height in the free soundings in Seville (Section 3.3).

Large-scale tropospheric subsidence over the area, which leads to higher O_3 concentrations in the boundary layer (see Gaudel et al., 2018 and references therein) might have also contributed to the increase in O_3 levels during the campaign. These episodes, associated with large-scale tropospheric subsidence, very frequently occur over the Mediterranean during the warm period of the year, in association with high-pressure systems, and are not always necessarily related to stratospheric intrusions (Coman et al., 2012; Doche et al., 2014; Eremenko et al., 2008; Foret et al., 2009; Richards et al., 2013; Safieddine et al., 2014; Tombrou et al., 2015; Zanis et al., 2014). In fact, the meteorological maps (Figs. 2 and S3) indicate that an extended tropospheric subsidence event probably occurred over the area during the examined episode of July 9th to 11th, 2019.

3.2. Surface O_3 and NO_2 concentrations

CALIOPE simulated a progressive accumulation of O_3 in the southern half of the Iberian Peninsula from July 8th to 11th, with prominent peaks between 12:00 and 20:00 UTC, which gradually became depleted on July 12th and 13th. The accumulation processes of O_3 were described in detail by Millán et al. (1997, 2002) and Gangoiti et al. (2001) for the Western Mediterranean area. These papers showed that pollutants are transported inland by sea-breeze and valley circulations caused by weakened synoptic surface circulation and the Iberian and Saharan thermal lows. In the case of the GV, the sea breezes transport air masses inland towards the Sierra de Cazorla mountain range, which creates a chimney/crest effect, injecting polluted air masses up to 2000 to 3000 m a.s.l. In the situation where the boundary layer is below the head of the valley, a pocket is formed that traps the air masses by thermal inversion of the top of the boundary layer, and the air masses are recirculated back towards the ocean. At the ocean, the air masses will sink due to compensatory subsidence. The combination of the recirculation, fumigation, and breeze transport results in accumulation occurring in the valley and generates acute O_3 episodes. This process will continue until the synoptic flow intensifies and vents the valley by transporting the polluted air masses to other areas (Gangoiti et al., 2006).

The regional accumulation of O_3 until July 11th at 12:00 UTC and the final venting stage of the GV were reproduced with the CALIOPE measurements, as seen in Section 3.3. The modeling also showed that O_3 transported from the Cantabrian and Portuguese coasts was channeled into the GV from the Atlantic. Regional O_3 formation was widespread between July 8th and 11th, with strong activity not only in the GV but also in the central and eastern parts of Iberia (Fig. S6).

The accumulation over the 3 days was also measured by the AQMSs in the GV during the campaign period. All stations showed a clear increasing trend of maximum daily O_3 concentration from July 8th until July 11th, 2019, with an average maximum O_3 concentration of 95 μg/m^3 on July 8th to 138 μg/m^3 on July 11th (Table S6). At the same time, when looking at certain stations, the hour of the maximum concentration progressively increases from west to east (Fig. S7). From the La Orden station near Huelva to the Las Fuentezuelas station near Jaén, there is a three-to-four hour delay between the hours with the maximum O_3 concentrations per day. This trend follows the dynamic of a sea breeze, as explained earlier in this section. Although a few stations do follow this trend, it is important to note that this was only seen at select stations and not at all stations inside the valley. This trend was also observed at the EMEP AQMS of Doñana, representing the background GV concentrations in the coastal area (Escudero et al., 2016), which supports the occurrence of vertical recirculation and accumulation during the campaign. The daily progressive accumulation of O_3 was more prevalent at the western AQMSs than at the eastern ones, where peak concentrations tended to occur later in the day (16:00–17:00 UTC) due to the transportation of polluted air masses by sea breezes, after the onset of the easterlies at lower atmospheric levels in the Strait of Gibraltar (Section 3.1).

Column NO_2 data from TROPOMI (Fig. S8) indicate that the highest levels in the GV were recorded in and around Seville, and not in the industrial area of Huelva. At the same time, there was a significant source of NO_2 a few kilometers offshore of the Guadalquivir estuary, due to the intense maritime traffic over the Atlantic in front of the GV (especially on July 11th), which likely favored the formation of O_3 production that was then transported inland by the sea breezes.

3.3. Vertical and horizontal O_3 profiles

3.3.1. July 9th, 2019

3.3.1.1. Morning. The GV was ventilated well in the days prior to July 9th, 2019 (Section 3.1), resulting in reduced O_3 levels in the area, with background O_3 being supplied mostly from the Atlantic. At 06:00 UTC (Fig. 3a) on July 9th, 2019, the sounding shows that surface O_3 reached the lowest values during the campaign (with titration, ozonolysis, and deposition occurring in a thin mixing layer). Four O_3 strata are evident in the profile. Below 600 m a.s.l., where there was a thermal inversion, the atmosphere was characterized by north-northeasterly katabatic winds and a marked O_3 reduction all the way down to the surface. The layer between 600 and 1800 m a.s.l. was characterized by northwesterly winds, with increasing RH and constant O_3 (around 50 ppb). From 1800 to 3250 m a.s.l., another O_3 increase was observed, with moderate and increasing northwesterlies, which backed to the west at higher altitudes. Above 3250 m a.s.l., the troposphere became dryer above a slight thermal inversion, but the westerly circulation was maintained, with a

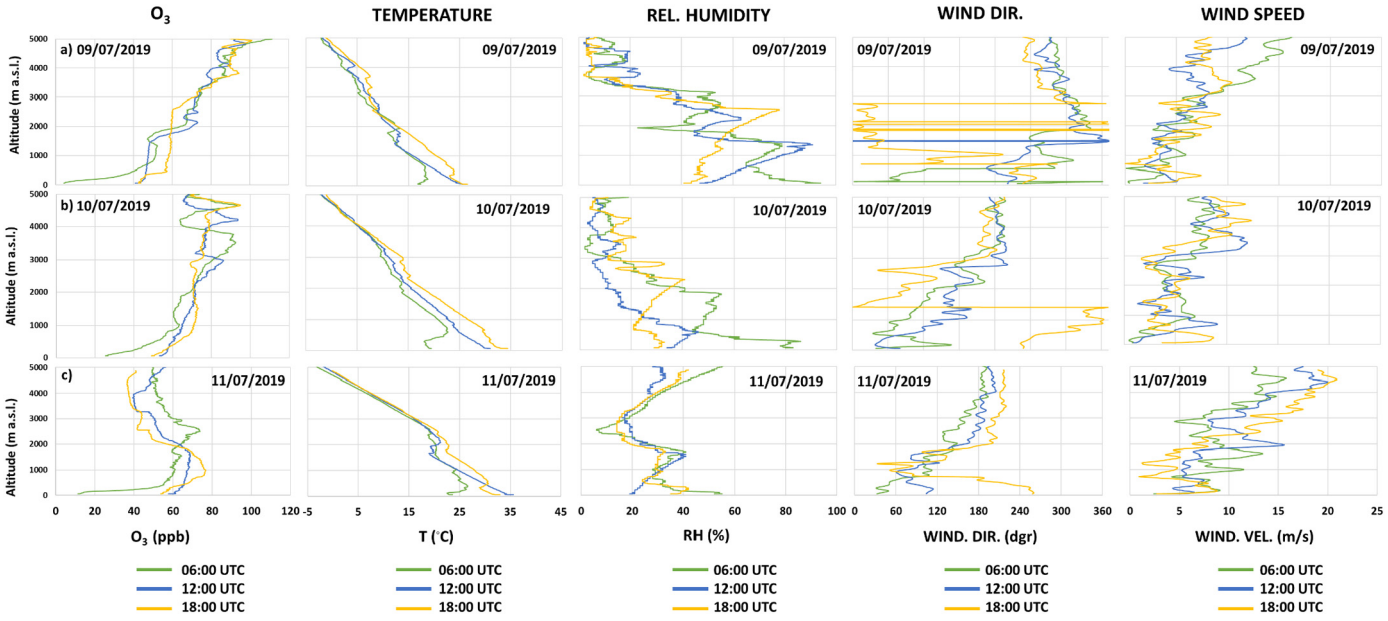

Fig. 3. Results of the O_3 and meteorology soundings on the three campaign days with the levels of O_3, temperature, relative humidity, wind direction, and wind speed up to 5000 m a.s.l. for a) July 9th, b) July 10th, and c) July 11th.

progressive increase in O_3 of up to 100 ppb at 5000 m a.s.l. This low RH and the very high and thick O_3 layer were likely influenced by the stratospheric O_3 intrusion described above, although stratospheric subsidence might also have contributed to increase O_3 levels. The upper-level low-pressure system located west of Portugal generated a westerly and northwesterly flow at this altitude and transported stratospheric O_3 from higher altitudes during this day. In summary, there was a clear gradual upward increase in O_3 along the profile.

3.3.1.2. Afternoon. At 12:00 UTC (Fig. 3a), surface O_3 increased compared with the morning (<400 m a.s.l.). A second layer persisted on top of the mixing layer (400–1400 m a.s.l.) with a thermal inversion at the top, a nearly constant O_3 concentration of ~45 ppb, a prevalent sea breeze (southwesterly) flow, and a high and increasing RH. From 1400 to 1800 m a.s.l., a transitional O_3 layer was observed, which was the entrainment zone of the convective boundary layer (CBL), limited by two thermal inversions, with a rising O_3 concentration (40 to 70 ppb) and decreasing RH. The top inversion occurred in the morning at 1700–1900 m a.s.l. Above 1800 m a.s.l., a layer with a moderate but increasing O_3 level was detected with northwesterly flow. The top layer was characterized again with a high upward O_3 increase (up to 100 ppb at 5000 m a.s.l.) and a 3900–4100 m a.s.l. thermal inversion. All three O_3 strata above 600 m a.s.l. were similar to those of the morning, but they were now located at lower altitudes. Furthermore, the concentrations of O_3 were high at high altitudes with a northwesterly wind, similar to the 06:00 UTC sounding, as a consequence of the persistence of the contribution from the stratospheric O_3 intrusion, probably with a low incidence of surface O_3.

3.3.1.3. Evening. Three well-defined strata were identified in the 18:00 UTC sounding (Fig. 3a). The lower layer (<350 m a.s.l., limited by a thermal inversion) had a persistent southwesterly sea-breeze flow, but simultaneously O_3 increased to around 40 ppb, similar to its level at 12:00 UTC. Another layer (350 to 2700 m a.s.l.) with northerly and northeasterly winds, high RH, and a homogeneous O_3 concentration of 65 ppb was probably the mixing layer and was associated with the northwesterlies of the cold advection at the rear of the upper-level low #1 (mentioned earlier in Section 3.1) (Fig. S3). This was channeled into the GV and contained a fraction of the pollutants moving inland within the sea breeze at lower levels, and was then transported back to the Atlantic as shown by the wind direction in the vertical profiles (Fig. 3a). Above 2700 m, the high O_3 concentrations from possible stratospheric intrusions or atmospheric subsidence O_3, high-speed westerly flow, and low RH persisted, with an upward increase of O_3 (again up to 100 ppb at 5000 m a.s.l.).

3.3.2. July 10th, 2019

3.3.2.1. Morning. On the morning of July 10th, the four-layer O_3 structure resembled that of the previous morning (Fig. 3b), including the upper layers with O_3 peaks reaching 90 ppb, high and stable wind speeds (7–8 m/s) from the southwest, and very low RH. The low RH and the high O_3 levels were likely associated with the stratospheric intrusion, which was also recorded the day before, but the results of the July 10th measurements showed traces of disruption and a decrease in O_3 compared with the previous day, which is consistent with the transitional character on this day for the stratospheric intrusions reported in Section 3.1.

3.3.2.2. Afternoon. The afternoon atmosphere profile (Fig. 3b) was very similar to the one of the morning sounding, but the layers were at lower altitudes. The thermal inversion was located at 900 m a.s.l., which indicates a much less developed boundary layer compared to the previous day. Below the thermal inversion, northeast to southeast winds prevailed with increasing speeds (2–8 m/s) and decreasing RH (down to 35%). Concentrations of O_3 were higher (55–63 ppb) in this lower layer compared to the morning sounding due to vertical mixing, but also possibly due to local production. Above the thermal inversion, up to 2700 m a.s.l. there was a dominant layer with southeasterly flow (5 m/s), a decrease in RH (down to 10%), and increased O_3 (55 to 85 ppb). Finally, above 2700 m a.s.l, there was a stable southwesterly wind (8–10 m/s), with two high O_3 strata (up to 90 ppb).

3.3.2.3. Evening. Three layers were detected during the evening sounding (Fig. 3b). The lower layer was limited by a thermal inversion at 600 m a.s.l. and characterized by low RH (35%) and southwesterly sea-breeze flows with low wind speeds, with an O_3 increase from 55 to 70 ppb. Similar to the prior day's sounding, a very well-mixed layer with a homogenous O_3 concentration of about 70 ppb was detected from 600 to 2300 m a.s.l. This layer showed a moderate RH (20 to 40%

from bottom to top) and northeasterly wind direction, which is consistent with the shift from westerlies to easterlies observed in the morning sounding. Just as on the previous evening, the northeasterlies transported the pollutants towards the Atlantic Ocean, from which the sea breeze could then carry them into the valley again at lower levels on the following morning, as was seen with the increased O_3 concentrations throughout the day at these altitudes compared with the previous day. Above 2300 m a.s.l., following the warm advection induced by the upper level low #2, the wind veered from southeast to southwest. Higher wind speeds were measured around 9 m/s, with low RH, and O_3 increasing slightly up to about 75 ppb, which was lower than the values attained in the morning and on previous days.

3.3.3. July 11th, 2019

3.3.3.1. Morning. During the morning of July 11th (Fig. 3c), the three layers were still persistent, with the bottom layer limited by the thermal inversion at 500 m a.s.l. The second layer (500–2500 m a.s.l.) was composed of several thinner strata associated with high and increasing O_3 concentrations (from 55 to 75 ppb) and a RH of 25–35%. From bottom to top, the wind (7–9 m/s with peaks of up to 13 m/s) veered from northeast to southeast. From 2500 to 5000 m a.s.l., O_3 decreased down to 50–60 ppb, with winds veering from southeast to southwest (10–12 m/s). There was also an increase in RH with altitude, indicating a different origin for the air masses that replaced the stratospheric-intrusion–related O_3 transported from previous days. Also, the northeast to southeast airflow in the 500–2500 m a.s.l. layer suggests that the Mediterranean is the origin of the air masses, as described in Section 3.1.

3.3.3.2. Afternoon. The three main layers were still persistent at 12:00 UTC (Fig. 3c). The lowest and second layers were limited by thermal inversions at 400 and 1600 m a.s.l. The lower level was characterized by low RH (increasing upward from 20 to 35%) and east-northeasterly winds (probably driven by the Mediterranean air mass transport) of around 5 m/s. This is similar to the second layer on July 10th, but with a thicker mixing layer. Interestingly, the O_3 concentration in this layer was higher than in the layers above, resulting in a 50–60 ppb "hump" in the profile (more pronounced in the sounding). This hump was likely caused by a combination of O_3 fumigation from mid-altitude reservoir strata and the residual layer of locally-produced O_3 from previous days (Escudero et al., 2019; Querol et al., 2017, 2018), along with O_3 transported from the Mediterranean. This hump was even more pronounced in the evening profile. In the 1600–5000 m a.s.l. layer, the high-speed (13–20 m/s) south-southwesterly wind prevailed in an air mass with low RH (25%) and lower and constant O_3 concentrations (around 50 ppb).

3.3.3.3. Evening. The same three strata were observed in the last sounding (Fig. 3c). In the lower layer, the southwesterly sea breeze was more intense than on the previous day (7–8 m/s and 40% RH). In this layer, O_3 concentrations increased from 55 to 70 ppb. In the middle layer (400 to 1750 m a.s.l.), a mixing layer with high levels of O_3, up to 75 ppb formed the aforementioned hump. This layer was driven by very low-speed east-northeasterly winds (2–4 m/s) originating from the Mediterranean region. This air mass could also recirculate back into the Atlantic, where the southwesterly sea breeze could transport it back into the GV at lower levels. As stated earlier, the effects of the air mass vertical recirculation and the background O_3 concentrations transported from the Mediterranean may have been important contributors to the measured O_3 hump. Above 1750 m a.s.l., O_3 concentrations decreased and remained stable at around 40 ppb. This air mass was affected by high-speed winds (18–20 m/s) with a constant southwesterly wind. The RH increased from 15 to 40%.

3.3.4. Agricultural biomass burning and African dust outbreak

The morning microlight measurements of July 9th, 2019 (Fig. 4a) showed a prominent increase in $PM_{2.5}$ and BC up to 185 and 1.5 μg/m^3, respectively, in the northeast sector of the flight (Seville-Lora del Rio, in the green box in Fig. 4d). The UFP data were unavailable from this flight due to instrument failure. These peaks coincided with widespread agricultural burns in the area (see Fig. S9) and with an O_3 decrease of 15 ppb (down from 45 ppb measured in the other GV areas, Fig. 4a). We do not have a reference for the timing and frequency of the burns, but in the early morning the boundary layer was much thinner and the contaminants from these burns had clearly accumulated and were consuming O_3 more intensively. Visual observations and RH data also revealed the occurrence of fog over this area. This fog most likely originated from the wide section of the river, which provides high humidity at the surface level, in combination with an abundance of irrigated green crops in this area. Both the fog and the biomass burning might have caused the O_3 decrease, given the inverse relationship between high RH and O_3 and the emissions of pollutants, with potential O_3 titration and/or ozonolysis effects (Carter et al., 1999; Granier et al., 2000; Jia and Xu, 2014). Later in the afternoon (Fig. 4b), $PM_{2.5}$, BC, and UFP were still detected in the same area (30 and 0.8–1.2 μg/m^3, 7000–17000 #/cm^3, respectively), but in contrast to the morning, there was a significant increase in O_3 (by up to 15 ppb, compared with 50–55 ppb background in other areas) at decreasing altitudes. Thus, biomass burning emissions and fog caused O_3 depletion during the morning, while the first simultaneously provided precursors that generated O_3 at lower altitudes in the afternoon. During the evening (Fig. 4c), O_3 concentrations were relatively constant at around 45 ppb, lower than in the afternoon (50–55 ppb). A homogeneous air mass resulting from convective processes and breeze circulations filled the GV. UFP levels remained relatively high (7500 #/cm^3) over the area where agricultural burns were located, although lower than during the morning and afternoon flights (10000–14000 #/cm^3). Thus, on this day, agricultural biomass burning contributed to increased background levels of UFP and O_3 to the northeast of Seville.

During the second day (July 10th, 2019) the impact of biomass burning on the air quality persisted in the northeast section of the morning flight (Fig. 5a), with high levels of $PM_{2.5}$, BC, and UFP (40 μg/m^3, 0.5 μg/m^3, and 6000 #/cm^3), and again a decrease of 10 ppb in O_3 with respect to the surrounding background levels was detected. However, during the afternoon, the O_3 formation in this northeastern transect was less pronounced than that of the previous day (Fig. 5b).

During the morning flight (Fig. 6a) of the last day (July 11th, 2019) the impact of biomass burning over the northeastern transect was evidenced again (70 and 2.9 μg/m^3 of $PM_{2.5}$ and BC, respectively; no UFP data were available due to an instrument failure). During the evening flight (green squares in Fig. 6c and f), it was possible to visually identify an African dust layer that slightly affected the study area (Fig. S10), increasing the $PM_{2.5}$ background levels from 20 to 28 μg/m^3. This impact may have been stronger for PM_{10} than for $PM_{2.5}$ (Querol et al., 2019).

3.3.5. Urban and industrial plumes

During the beginning of the afternoon flight on the first day (July 9th, 2019, Fig. 4b), increases in O_3 (up to 15 ppb over a constant background of 45 ppb) and UFP (10000 #/cm^3 over 2000 #/cm^3) concentrations were measured on the approach to Seville due to the emissions of the city, as was confirmed with HYSPLIT modeling (black squares in Fig. 4e). During the afternoon flight, high levels of pollutants (60 μg/m^3 and 30000–100000 #/cm^3 of $PM_{2.5}$ and UFP, respectively, together with a slight increase in O_3 of 7 ppb) were also recorded over northeast Huelva when crossing the plume of the petrochemical plant, as was confirmed by HYSPLIT modeling (red squares in Fig. 4e). The evening flight (Fig. 4c) also measured an 8 ppb O_3 increase when crossing the plume of the petrochemical plant (red squares in Fig. 4f), while at the same time significant increases in $PM_{2.5}$ and UFP levels were detected (32–35 μg/m^3 and 17000–22000 #/cm^3, respectively).

In the morning flight of the second day (July 10th, 2019, Fig. 5a), a very high peak in UFP (up to 120000 #/cm^3) and low BC levels, without a major effect on O_3, were measured over the southeast of Huelva, coinciding with the petrochemical plume transport (red squares in Fig. 5d).

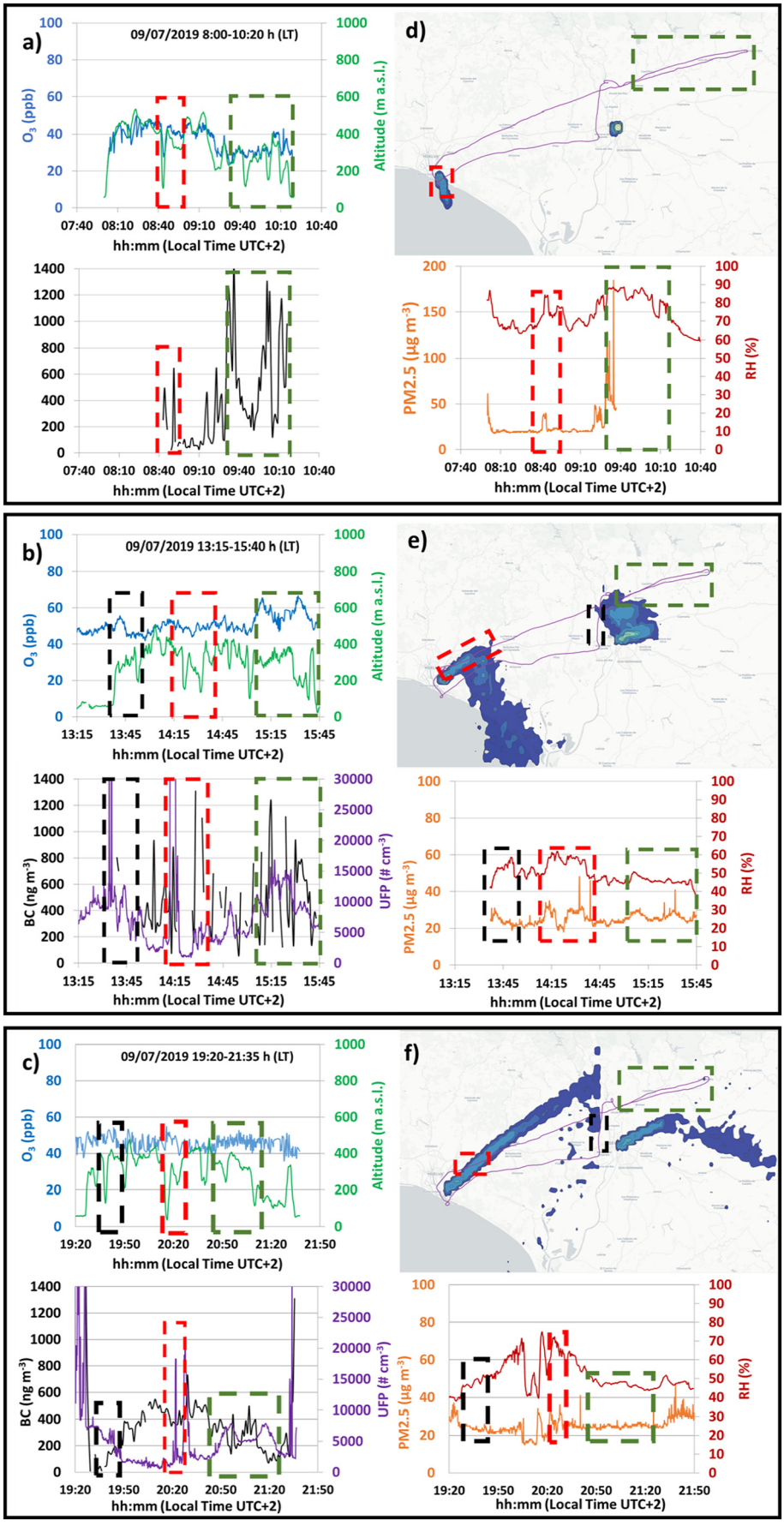

Fig. 4. Concentrations of O_3, BC, UFP, $PM_{2.5}$, RH, and altitude measured during the: a) morning, b) afternoon, and c) evening microlight flights of July 9th, 2019, and HYSPLIT modeling of the plume transport of the Huelva petrochemical plant and Seville City (d, e, and f) during the respective flights.

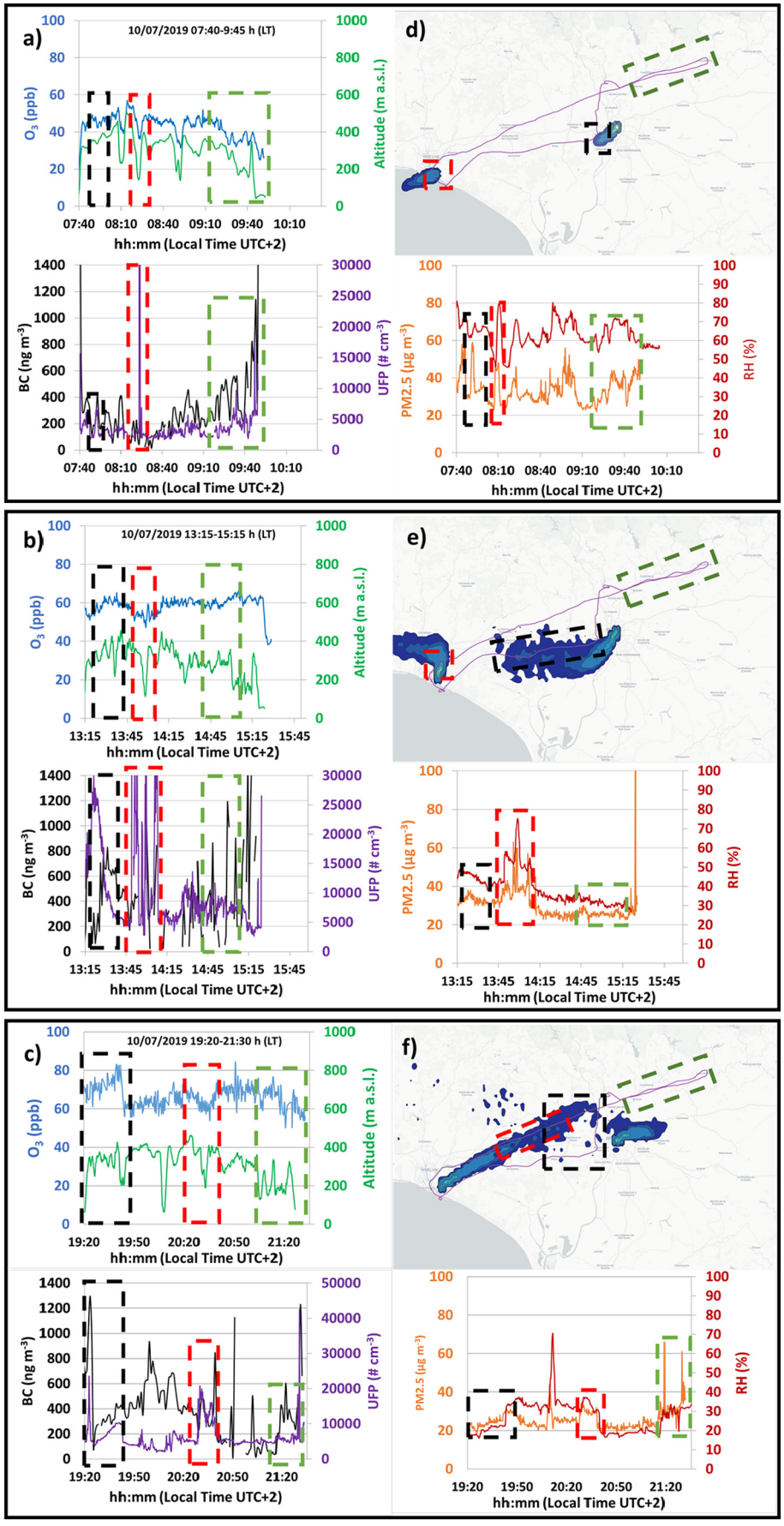

Fig. 5. Concentrations of O_3, BC, UFP, $PM_{2.5}$, RH, and altitude measured during the: a) morning, b) afternoon, and c) evening microlight flights of July 10th, 2019, and HYSPLIT modeling of the plume transport of the Huelva petrochemical plant and Seville City (d, e, and f) during the respective flights.

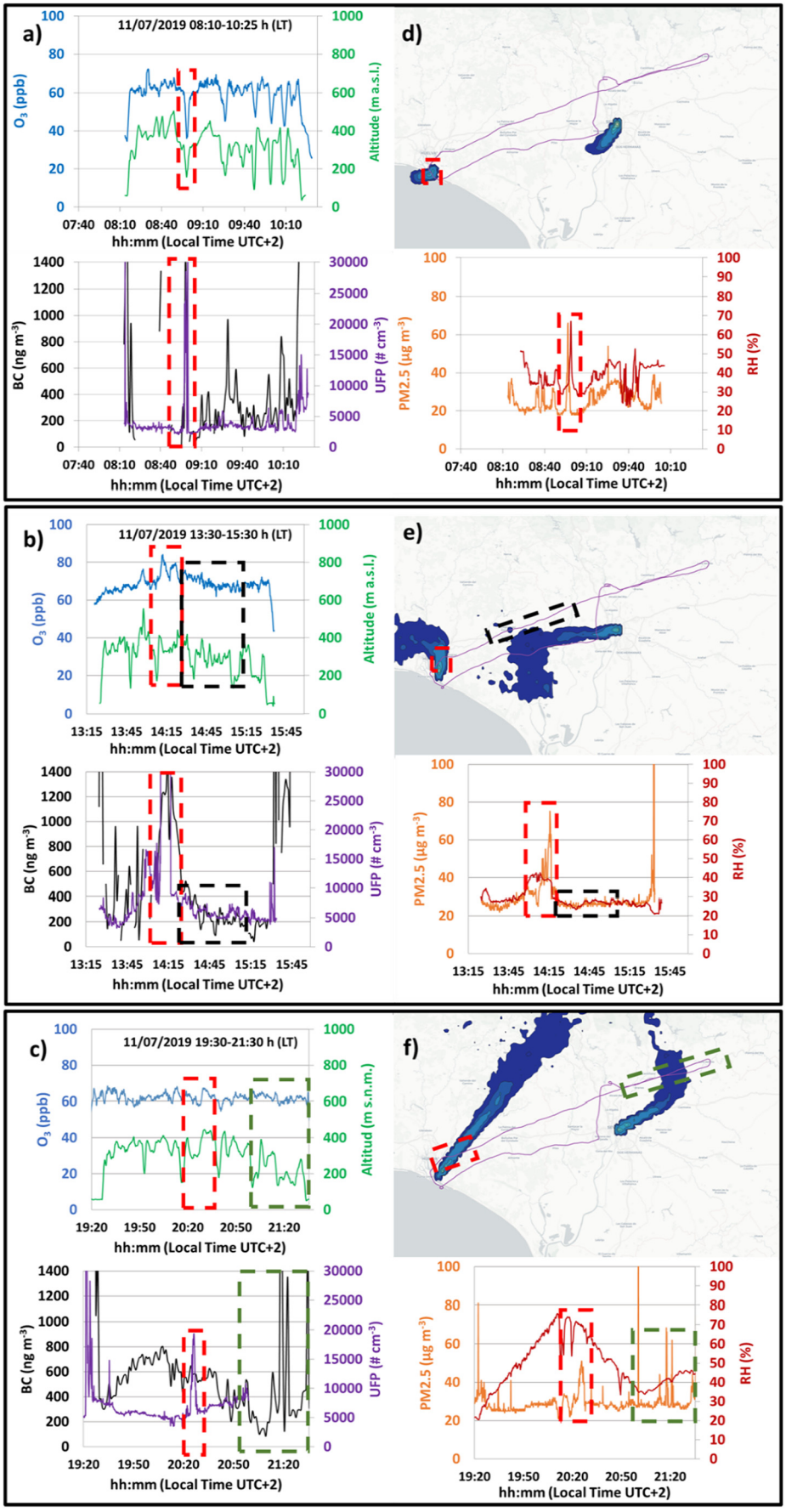

Fig. 6. Concentrations of O_3, BC, UFP, $PM_{2.5}$, RH, and altitude measured during the: a) morning, b) afternoon, and c) evening microlight flights of July 11th, 2019, and HYSPLIT modeling of the plume transport of the Huelva petrochemical plant and Seville City (d, e, and f) during the respective flights.

There was also a moderate peak in UFP over Seville (6000 #/cm^3) (black squares in Fig. 5d), along with increases in $PM_{2.5}$ and BC (60 and 0.4 μg/m^3, respectively), but no significant changes in O_3 concentrations. During the afternoon (Fig. 5b), O_3 concentrations increased when approaching the plume of Seville (black squares in Fig. 5e), while simultaneously $PM_{2.5}$ and BC concentrations increased to 38 μg/m^3 and 0.7 μg/m^3, respectively, and UFP concentrations decreased from 26000 #/m^3 to 10000 #/m^3. A decrease of 10 ppb O_3 was measured over the petrochemical plant (red squares in Fig. 5e) along with extremely high peaks of UFP (21000 to 104000 #/cm^3) as in the morning, which coincided with higher $PM_{2.5}$ and BC peaks (65 and 1.2 μg/m^3). These increases coincided with the rapid descent of the plane to 150 m a.s.l., which might be the cause of the increases and decreases detected. During the evening (Fig. 5c), O_3 increased by 25 ppb to the west of Seville (black squares in Fig. 5f). The interesting thing about this increase is that the modeled plume does not coincide with this area but UFP and BC were observed to be 10000 #/cm^3 (compared with a background of 2000 #/cm^3) and 0.8 μg/m^3, respectively, which points towards a local origin from the residual plume of Seville, the Huelva petrochemical plant, or biomass burning. When crossing the plume of Huelva (red squares in Fig. 5f), increased levels of $PM_{2.5}$, UFP, and BC were measured, with concentrations reaching 30 μg/m^3, 0.8 μg/m^3, and 20000 #/cm^3, respectively, but with a decrease of 7 ppb O_3. As with the previous flight, this did coincide with a decrease in altitude that might be the cause of these observations, although the concentrations recorded in this plume were comparable to the levels recorded by the AQMSs, even when the plane descended to 200 m a.s.l.

The morning flight on the last day (July 11th, 2019, Fig. 6a) recorded a constant O_3 concentration of 65 ppb at 300 m a.s.l., which was higher compared to the morning flights of the previous days (45 ppb). Peak UFP, $PM_{2.5}$, and BC concentrations (47000 #/cm^3, and 200 and 1.4 μg/m^3, respectively) were measured over the plume of Huelva (red squares in Fig. 6d) due to the rapid decrease in altitude of the plane, which also affected the O_3 concentrations. The afternoon flight (Fig. 6b) sampled the highest levels of O_3 detected by the flights during the campaign. Background O_3 levels of 65–68 ppb were recorded at 300 m a.s.l., and a 20 ppb increase was evident when crossing the plume of Huelva's petrochemical plant (red squares in Fig. 6e), together with high concentrations of UFP, $PM_{2.5}$, and BC (140000 #/cm^3, and 80 and 1.6 μg/m^3, respectively). Furthermore, when crossing the plume of Seville (black squares in Fig. 6e), O_3 levels also increased by up to 10 ppb, while the rest of the pollutants remained at background levels. The evening flight (Fig. 6c) was affected by the venting meteorological change described in Section 3.1, which caused a decrease in the O_3 regional background concentrations (down to 62 ppb of O_3 at 300 m a.s.l.) compared with the previous flight. Concentrations of O_3 were homogeneous throughout the GV without increases associated with urban and industrial plumes (Fig. 6f), but over the Huelva plume, peak UFP and $PM_{2.5}$ concentrations (up to 17000 #/cm^3 and 50 μg/m^3, respectively) were still recorded.

4. Discussion

Data from the AQMSs showed a progressive accumulation of O_3 in the GV from July 9th to 11th, 2019, with the maximum being reported in the hours when fumigation from upper high-O_3 strata, O_3 formation, and O_3 transport by sea breezes were at their maximum. This scenario was similar to those of other locations in Spain, as was described for the Morella-Castelló (Gangoiti et al., 2001), Vic-Barcelona (Millán et al., 2002), and Madrid atmospheric basins (Escudero et al., 2019; Querol et al., 2018).

Three to four O_3 layers were identified every day in the first 5000 m a.s.l., with the altitudes of the layers subsiding in the afternoon and evening compared with the morning. This difference is caused under anticyclonic conditions and clear skies, by the lower layers warming up during daytime, and consequently expand in altitude, while during nighttime the lower layers will cool down and shrink. This subsidence intensified from July 9th until 11th as can be seen by the vertical temperature and humidity anomalies in Fig. 3. Fig. 7 shows the evolution of the average O_3 concentrations recorded by the soundings for four groups of layers located at different altitudes from July 9th to 11th, according to the morning, afternoon, and evening profiles. The accumulation occurred mainly between 400 and 1850 m a.s.l., where O_3 concentrations reached up to 75 ppb during the afternoon and evening soundings of July 10th and 11th, giving rise to a hump-shaped O_3 profile (Fig. 3b and c).

We suggest two major processes to be the origin of this hump. First, the surface sea breeze drew O_3 and its precursors to the interior of the GV. These pollutants were then injected at mid-altitudes by the higher topography of the upper valley, and were vertically recirculated towards the ocean (Gangoiti et al., 2001; Millán et al., 1997, 2002; Pay et al., 2019). In the GV, airmasses were driven by easterly winds (2–4 m/s and RH < 50%) during July 10th and 11th and were channeled into the GV in a northeast-to-southwest direction during the evening of the campaign. Afterward, the air masses would flow

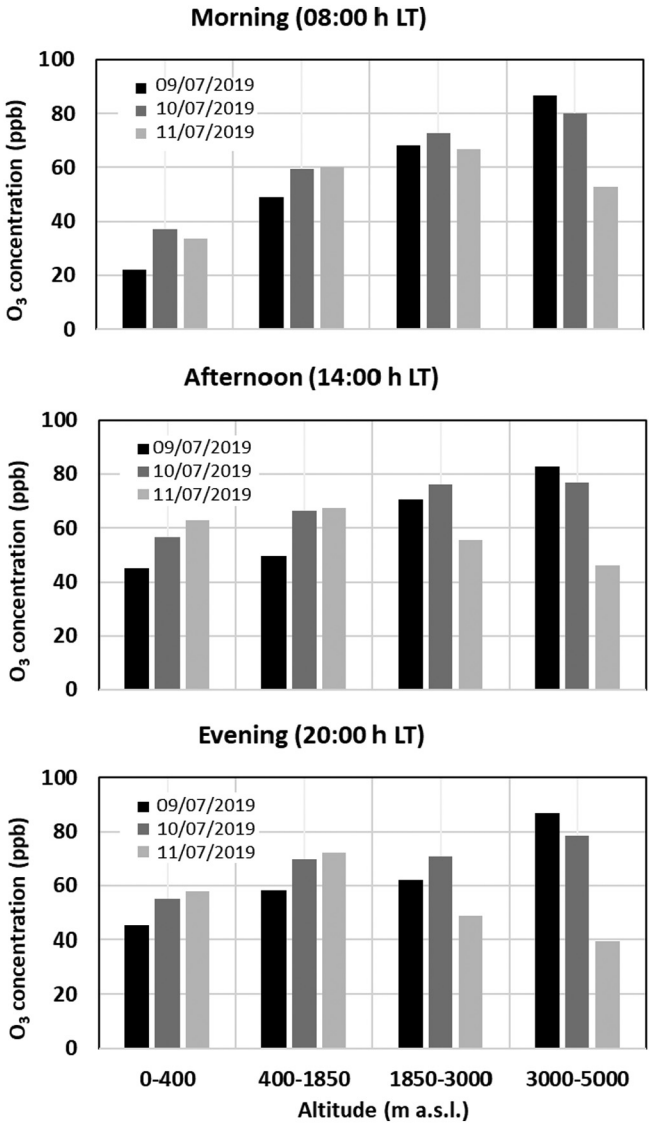

Fig. 7. Time evolution of the average O_3 levels measured during the morning, afternoon, and evening soundings for four layers (0–400, 400–1850, 1850–3000, and 3000–5000 m a.s.l.) from July 9th to 11th, 2019.

over the southwesterlies of the sea breeze after full development of the convective recirculation inside the valley. This situation was similar to the episodes of high O_3 in the Madrid Basin, where the O_3 episodes were generated by the vertical recirculation of air masses, caused when the boundary layer at midday reached a lower altitude than the Sierra de Guadarrama. This trapped regional air masses in the basin, which generated a similar mid-altitude O_3 hump (Querol et al., 2018). Second, the change in the mid-altitude synoptic flow, from westerlies (July 9th) to easterlies (July 10th and 11th), probably contributed to an increase in O_3 concentrations (from the second half of July 10th) by transporting polluted air masses into the region from the Eastern and Southeastern Mediterranean. This accumulation would be enhanced further by a progressive increase in insolation and temperature, with a temperature increase of 8 °C to 10 °C during the campaign, depending on the time of day, promoting additional O_3 formation. Finally, Lefohn et al. (2012), Parrish et al. (2012), Kalabokas et al. (2013, 2015) Zanis et al. (2014), and Akritidis et al. (2016), among others, reported relevant contributions from stratospheric intrusions and tropospheric subsidence to surface O_3 concentrations in the Eastern Mediterranean, Middle East, and United States background O_3 levels. Also in the Western Mediterranean, Kalabokas et al. (2017) reported that during springtime O_3 episodes (April–May), O_3 subsidence from the upper levels may affect the boundary layer as well as the ground surface O_3 concentrations due to vertical mixing through the entrainment zone of the boundary layer (Pay et al., 2019). In the case of the GV, at the highest altitudes (3000–5000 m a.s.l.), O_3 clearly decreased over the three-day period, with the O_3 concentrations being reduced by half on July 11th compared to July 9th in all soundings (morning, afternoon, and evening). This decrease also occurred on the last day for the layers between 1850 and 3000 m a.s.l. This would signify that if stratospheric intrusion occurred, its impact would be less significant over time.

At the surface, O_3 increased in the GV due to surface fumigation from the high-O_3 mid-altitude layer, formation and horizontal transport by sea breezes, and higher temperatures. During the campaign, an accumulation of O_3 occurred over 2.5 days (from July 9th until July 11th), and concentrations increased from 45 to 62 ppb at the surface at Aljarafe Mairena (southwest of Seville), and from 50 to 75 ppb at 400–1850 m a.s.l. during the afternoon soundings. Thus, the increase was mainly due to local and regional causes and was approximately 20 ppb during the study episode. This was also confirmed by airborne measurements carried out simultaneously with the microlight flights, which measured a generalized increase of 20–21 ppb O_3 at 300 m a.s.l. across the GV (Fig. 8).

The combination of decreasing O_3 at highest altitudes and increasing O_3 at lower altitudes, along with the subsidence of the upper layers over the three days and mixing between these layers, resulted in a progressive homogenization of the profiles. For example, on July 9th, the difference increased from around 40 to 100 ppb O_3 between 0 and 5000 m a.s.l., while the difference increased only from 50 ppb to 70 ppb on July 10th. This occurrence is supported by the temperature profiles (Fig. 3), which show a temperature inversion across the top of the boundary layer (Fowler and Brooks, 2006; Kaser et al., 2017), and the inverse trend of the 400–1850 and < 400 m a.s.l. layers, which shows a clear and progressive accumulation of O_3. Thus, without discarding the influence of subsided stratospheric O_3, we believe that the increase in O_3 regional background levels at lower atmospheric levels was mostly driven by other regional atmospheric processes. Large-scale tropospheric subsidence over the area might have also contributed to an increase in O_3 concentrations in the boundary layer. However, to quantify the proportions of O_3 contributed by recirculation, by formation and transport, and by atmospheric subsidence, only modeling tools are needed, which is beyond the scope of this article. However, on July 11th, the O_3 profiles showed a clear hump into the boundary layer, with minimal O_3 levels above this (2500–3000 m a.s.l., Fig. 3c), pointing to the typical regional episodes described across Iberia by Gangoiti et al. (2001), Millán et al. (1997, 2002), and Querol et al. (2017, 2018), among others.

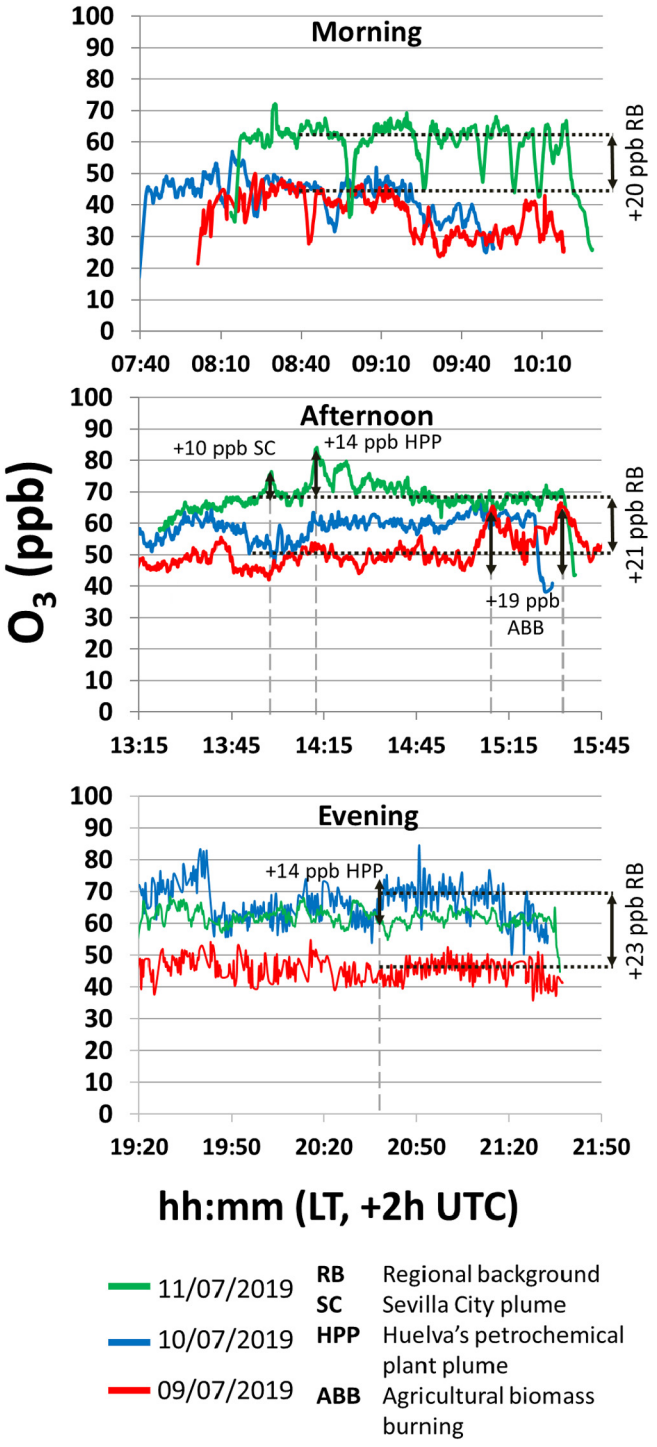

Fig. 8. Comparison of the O_3 concentrations during the flights of the morning, afternoon and evening from July 9th to 11th 2019.

Furthermore, the microlight flights in combination with HYSPLIT modeling allowed quantification of the O_3 contributions from specific sources (on top of the O_3 background), such as the pollution plumes of the Huelva petrochemical plant and the city of Seville, as well as from the aging of agricultural biomass burning emissions.

Emissions from the early morning agricultural burns on July 9th from Seville to Lora del Río, and the fog in this agricultural area, produced a marked consumption in O_3 of 15 ppb during the morning flights on July 9th and 10th, 2019 (Figs. 4a and 5a). This was also described by Granier et al. (2000), who reported the impact on O_3 formation due to emissions of CO, NO_x, and hydrocarbons from biomass burning. The

emission of these precursors in the morning might have caused consumption of O_3 by titration of O_3 by NO and the ozonolysis of VOCs. However, in the afternoon the biomass burning yielded an increase in O_3 of 20 ppb (Figs. 4b and 8), together with increases in $PM_{2.5}$, BC, and UFP. Chen et al. (2017) reported that aging biomass plumes can induce the production of tropospheric O_3 as they contain an excess of O_3 precursors (VOCs, CO, NO_x), and found O_3 enrichment across China due to biomass burning. This was also reported by Zhu et al. (2014), who reported high concentrations of toluene, isoprene, ethene, propene, and n-hexane as well as their O_3 formation potential (OFP) in a rural area in Northern China with frequent biomass burns. Jaffe and Zhang (2017) also described delayed O_3 formation from wildfire plumes interacting with NO_x from urban plumes and attributed the delay to peroxyacetyl nitrate (PAN) present in the fire plumes.

Concentrations of O_3 in the plumes from Huelva's petrochemical plant and the city of Seville peaked (simultaneously with those of UFP and $PM_{2.5}$, and BC in some cases) mainly during the afternoon and evening flights. Thus, the afternoon and evening flights on July 9th measured an increase of 10 ppb O_3 over the regional background levels at 300 m a.s.l. (Fig. 8). An increase of 15 ppb was measured when crossing the Seville plume during the afternoon of July 10th (Fig. 8); finally, an increase of 10 to 17 ppb was measured during the afternoon and evening flights on July 11th through these plumes, reaching a maximum O_3 concentration of 85 ppb, which exceeded an already-high 68 ppb background during the afternoon of the same day (Fig. 8). Thus, both the modeling of the plume transports and the co-measurements of BC, $PM_{2.5}$, and UFP with O_3 allowed us to quantify the O_3 contribution from the plumes to the regional background O_3 background levels. Indeed, VOC and NO_x emissions from petrochemical plants may result in high O_3 formation rates. As an example, Fawole et al. (2017) measured peak concentrations ranging from 70 to 115 ppb in instrumented flights when crossing the plumes of a gas flare with high levels of CO and alkanes over the Niger Delta. As another recent example, in Xiong and Du (2020), six sources were identified in the Vancouver metropolitan area as contributing most of the VOC-related OFP, namely fuel production and combustion, fuel evaporation, vehicle exhaust, industrial coatings/solvents, a petrochemical source, and other industrial emissions, with the first three accounting for 68% of the OFP. However, high OFP has been widely reported when urban and industrial plumes interact with air masses containing high levels of biogenic VOCs (see as an example Zong et al. (2018) and references therein).

5. Conclusions

Intensive 3D measurements of O_3, $PM_{2.5}$, UFP, and BC concentrations, as well as meteorological parameters, were carried out with free soundings and instrumented microlight flights during an O_3 episode affecting the GV (southern Spain) between July 9th and 11th, 2019 to investigate the processes responsible for high O_3 pollution episodes in this region. The results suggest that the episode was caused by 2.5 days of local and regional O_3 accumulation. The main processes causing this accumulation were the:

(I) Transport from the Atlantic sector (western Iberia).
(II) Vertical recirculation of air masses by sea and valley breeze circulations interacting with complex topography.
(III) Locally-formed O_3 in the GV during July 9th and 10th, 2019.
(IV) Trans-basin contribution from Mediterranean O_3 during July 11th, which was initiated during the second half of July 10th.
(V) Possible atmospheric subsidence flows.

Background O_3 in oceanic air masses over the Gulf of Cádiz was transported inland by sea breezes, which drew O_3 and its precursors from the industrial and urban areas of Huelva, Seville, and Córdoba, causing O_3 maxima late in the afternoon–evening at the northeastern end of the GV. In fact, Castell et al. (2011) found the number of consecutive days with sea breezes to be the best predictor of O_3 accumulation processes in eastern Spain. Furthermore, upsloping winds at high altitude in the mountains of the eastern GV injected aged air masses into the mid-altitude (400–1850 m a.s.l.) troposphere (generating reservoir layers), which were transported back to the ocean within the northeasterlies, where they subsided and could be recirculated with the sea breezes of the following day (Fig. S11). Furthermore, on July 10th and 11th at this mid-altitude level (400–1850 m a.s.l.), air masses from the eastern to southeastern sectors (of Mediterranean origin) crossed the southern boundaries of the Betic System and reached the GV during the second half of July 10th (Fig. S5), likely bringing an additional supply of O_3. Surface fumigation from the recirculating reservoir layers and those of Mediterranean origin, vertical mixing through the entrainment zone of the convective boundary layer, and local plumes that were transported at lower levels together were the causes of the O_3 pollution episode observed during the field campaign. This resulted in an increase in O_3 over 2.5 days from an initial regional background concentration of 45 ppb on July 9th up to 70–75 ppb during the afternoon of July 11th, 2019.

On top of this gradual O_3 background increase, we quantified, with the support of $PM_{2.5}$, BC, and UFP measurements and HYSPLIT modeling, that local contributions increased the O_3 concentration by up to 20 ppb. Although the pollutants have various origins, the relative changes in concentration when crossing the pollution plumes and the agricultural burns made it clear that these were the sources of the observed changes. The attributed sources were agricultural burns and the transported plumes of Huelva's petrochemical plant and the city of Seville.

In the free troposphere, the stratospheric O_3 intrusion located over the region on July 9th was dispersed during July 10th and 11th, and the high O_3 concentration in the layer at 3000–5000 m a.s.l. followed an inverse trend to that described at the surface, decreasing by half on July 11th compared to July 9th (Fig. 7).

It is important to highlight that, in addition to the O_3 enhancement caused by agricultural burns, very high levels of BC, UFP, and $PM_{2.5}$ were measured regionally around these areas, especially to the northeast of Seville, which is an area with extensive agricultural practices. During the morning of July 9th and the afternoon of the 11th, abundant agricultural burns were evident, as well as black plumes derived from waste burning (plastics, tires, etc.). During the flights, we were even able to observe that an agricultural burn turned into an uncontrolled fire. We consider it necessary to abate these emissions, which have a strong impact on the air quality of the area.

Our results allowed us to develop a conceptual model of how high O_3 episodes occur in the GV, one of the areas of Spain with the highest O_3 levels after the Madrid and Barcelona regions. The results identified the key spatial patterns that modeling tools can use to accurately reproduce and forecast O_3 concentrations in the area, and to carry out sensitivity analyses to evaluate cost-efficient abatement measures. An important remaining gap in our knowledge is the evaluation of the actual species and concentrations of VOCs across the area horizontally and vertically, to further supply very relevant information to the modeling tools.

CRediT authorship contribution statement

M. in 't Veld: Investigation, Writing – original draft, Writing – review & editing, Visualization. **C. Carnerero:** Investigation. **J. Massagué:** Investigation. **A. Alastuey:** Methodology, Investigation. **J.D. de la Rosa:** Software, Investigation. **A.M. Sánchez:** Software, Investigation. **M. Escudero:** Investigation. **E. Mantilla:** Investigation. **G. Gangoiti:** Software, Investigation, Resources. **C. Pérez García-Pando:** Software, Investigation, Resources. **M. Olid:** Software, Investigation, Resources. **J.R. Moreta:** Investigation, Resources. **J.L. Hernández:** Investigation, Resources. **J. Santamaría:** Investigation, Resources. **M. Millán:** Resources. **X. Querol:** Conceptualization, Methodology, Investigation, Writing – review & editing, Visualization, Supervision, Project administration, Funding acquisition.

Declaration of competing interest

The authors declare that they have no known competing financial interests or personal relationships that could have appeared to influence the work reported in this paper.

Acknowledgments

The present work was supported by the Spanish Ministry for Ecological Transition (17CAES010); the "Agencia Estatal de Investigación" from the Spanish Ministry of Science, Innovation and Universities and FEDER funds under the project HOUSE (CGL2016-78594-R); the Agencia Estatal de Investigación (RTI2018-095937-B-I00); and the Generalitat de Catalunya (AGAUR 2017 SGR41). We would like to thank the Junta de Andalucía for providing us with air quality data, and the Spanish Met Office (AEMET) for providing meteorological data and facilitating staff and instrumentation for the soundings, as well as ESA for providing TROPOMI-NO_2 data and NOAA for the HYSPLIT modeling tool. Cristina Carnerero thanks "Agencia Estatal de Investigación" for the grant received to carry out her PhD (FPI grant: BES-2017-080027). Carlos Pérez García-Pando acknowledges support by the AXA Research Fund, and the Spanish Ministry of Science, Innovation and Universities (RYC-2015-18690).

Appendix A. Supplementary data

Supplementary data to this article can be found online at https://doi.org/10.1016/j.scitotenv.2020.144579.

References

Adame, J.A., Lozano, A., Bolívar, J.P., De la Morena, B.A., Contreras, J., Godoy, F., 2008. Behavior, distribution and variability of surface ozone at an arid region in the south of Iberian Peninsula (Seville, Spain). Chemosphere 70, 841–849. https://doi.org/10.1016/j.chemosphere.2007.07.009.

Adame, J.A., Bolívar, J.P., De la Morena, B.A., 2009. Surface ozone measurements in the southwest of the Iberian Peninsula (Huelva, Spain). Environ. Sci. Pollut. Res. 17, 355–368. https://doi.org/10.1007/s11356-008-0098-9.

Akritidis, D., Pozzer, A., Zanis, P., Tyrlis, E., Škerlak, B., Sprenger, M., Lelieveld, J., 2016. On the role of tropopause folds in summertime tropospheric ozone over the eastern Mediterranean and the Middle East. Atmos. Chem. Phys. 16, 14025–14039. https://doi.org/10.5194/acp-16-14025-2016.

Amann, M., Derwent, D., Forsberg, B., Hänninen, O., Hurley, F., Krzyzanowski, M., De Leeuw, F., Liu, S.J., Mandin, C., Schneider, J., Schwarze, P., Simpson, D., 2008. Health Risks of Ozone From Long-range Transboundary Air Pollution. World Health Organization.

Baldasano, J.M., Jiménez-Guerrero, P., Jorba, O., Pérez, C., López, E., Güereca, P., Martín, F., Vivanco, M.G., Palomino, I., Querol, X., Pandolfi, M., Sanz, M.J., Diéguez, J.J., 2008. Caliope: an operational air quality forecasting system for the Iberian Peninsula, Balearic Islands and Canary Islands – first annual evaluation and ongoing developments. Adv. Sci. Res. 2, 89–98. https://doi.org/10.5194/asr-2-89-2008.

Baldasano, J.M., Pay, M.T., Jorba, O., Gassó, S., Jiménez-Guerrero, P., 2011. An annual assessment of air quality with the CALIOPE modeling system over Spain. Sci. Total Environ. 409, 2163–2178. https://doi.org/10.1016/j.scitotenv.2011.01.041.

Banzon, V., Smith, T.M., Liu, C., Hankins, W., 2016. A long-term record of blended satellite and in situ sea surface temperature for climate monitoring, modeling and environmental studies. Earth Syst. Sci. Data Discuss., 1–13 https://doi.org/10.5194/essd-2015-44.

Bergin, M.S., Russell, A.G., Milford, J.B., 1998. Effects of chemical mechanism uncertainties on the reactivity quantification of volatile organic compounds using a three-dimensional air quality model. Environ. Sci. Technol. 32, 694–703. https://doi.org/10.1021/es9704489.

Carter, W.P.L., 2000. Documentation of the SAPRC-99 Chemical Mechanism for VOC Reactivity Assessment. Final Report to California Air Resources Board Contract 92-329 and Contract 95-308.

Carter, W.P.L., 2009. Updated maximum incremental reactivity scale and hydrocarbon bin reactivities for regulatory applications. Prepared for California Air Resources Board Contract 07-339.

Carter, W.P.L., Dongmin, L., Malkina, I.L., 1999. Investigation of the Atmospheric Ozone Formation Potential of Trichloroethylene. Final Report to the Chemical Manufacturers Association Diisocyanates Panel.

Castell, N., Stein, A.F., Mantilla, E., Salvador, R., Millán, M., 2009. Evaluation of the use of photochemical indicators to assess ozone-NOx-VOC sensitivity in the southwestern Iberian Peninsula. J. Atmos. Chem. 63, 73–91. https://doi.org/10.1007/s10874-010-9158-x.

Castell, N., Mantilla, E., Stein, A.F., Salvador, R., Millán, M., 2011. Simulation and evaluation of control strategies for ozone reduction in a complex terrain in southwestern Spain. Environ. Model. Assess. 16, 565–576. https://doi.org/10.1007/s10666-011-9265-3.

Chen, J., Li, C., Ristovski, Z., Milic, A., Gu, Y., Islam, M.S., Wang, S., Hao, J., Zhang, H., He, C., Guo, H., Fu, H., Miljevic, B., Morawska, L., Thai, P., LAM, Y.F., Pereira, G., Ding, A., Huang, X., Dumka, U.C., 2017. A review of biomass burning: emissions and impacts on air quality, health and climate in China. Sci. Total Environ. 579, 1000–1034. https://doi.org/10.1016/j.scitotenv.2016.11.025.

Colette, A., Aas, W., Banin, L., Braben, C.F., Ferm, M., Gonzalez Ortiz, A., Ilyin, I., Mar, K., Pandolfi, M., Putuad, J.-P., Shatalov, V., Solberg, S., Spindler, G., Tarasova, O., Vana, M., Adani, M., Almodovar, P., Berton, E., Bessagnet, B., Bohlin-Nizzetto, P., Boruvkova, J., Breivik, K., Briganti, G., Cappelletti, A., Cuvelier, K., Derwent, R., D'Isidoro, M., Fagerli, H., Funk, C., Garcia Vivanco, M., Haeuber, R., Hueglin, C., Jenkins, S., Kerr, J., de Leeuw, F., Lynch, J., Manders, A., Mircea, M., Pay, M.T., Pritula, D., Querol, X., Raffort, V., Reiss, I., Roustan, Y., Sauvage, S., Scavo, K., Simpson, D., Smith, R.I., Tank, Y.S., Theobald, M., Torseth, K., Tsyro, S., van Pul, A., Vidic, S., Wallasch, M., Wind, P., 2016. Air Pollution Trends in the EMEP Region Between 1990 and 2012. (EMEP: CCC-Report 1/2016). Norwegian Institute for Air Research, Kjeller.

Coman, A., Foret, G., Beekmann, M., Eremenko, M., Dufour, G., Gaubert, B., Ung, A., Schmechtig, C., Flaud, J.M., Bergametti, G., 2012. Assimilation of IASI partial tropospheric columns with an ensemble Kalman filter over Europe. Atmos. Chem. Phys. 12, 2513–2532. https://doi.org/10.5194/acp-12-2513-2012.

Dee, D.P., Uppala, S.M., Simmons, A.J., Berrisford, P., Poli, P., Kobayashi, S., Andrae, U., Balmaseda, M.A., Balsamo, G., Bauer, P., Bechtold, P., Beljaars, A.C.M., van de Berg, L., Bidlot, J., Bormann, N., Delsol, C., Dragani, R., Fuentes, M., Geer, A.J., Haimberger, L., Healy, S.B., Hersbach, H., Hólm, E.V., Isaksen, L., Kållberg, P., Köhler, M., Matricardi, M., Mcnally, A.P., Monge-Sanz, B.M., Morcrette, J.J., Park, B.K., Peubey, C., de Rosnay, P., Tavolato, C., Thépaut, J.N., Vitart, F., 2011. The ERA-interim reanalysis: configuration and performance of the data assimilation system. Q. J. R. Meteorol. Soc. 137, 553–597. https://doi.org/10.1002/qj.828.

Dentener, F., Keating, T., Akimoto, H., 2010. Hemispheric Transport of 2010: Part A - Ozone and Particulate Matter, Air Pollution Studies, No. 17. UN, New York https://doi.org/10.18356/2c908168-en.

Dieguez, J.J., Millán, M.M., Padilla, L., Palau, J.L., 2009. Estudio y evaluación de la contaminación atmosférica por ozone troposphericO en España.

Dieguez, J.J., Calatayud, V., Mantilla, E., 2014. Informe Final Memoria Técnica Proyecto CONOZE.

Doche, C., Dufour, G., Foret, G., Eremenko, M., Cuesta, J., Beekmann, M., Kalabokas, P., 2014. Summertime tropospheric-ozone variability over the mediterranean basin observed with IASI. Atmos. Chem. Phys. 14, 10589–10600. https://doi.org/10.5194/acp-14-10589-2014.

Dorman, C.E., Beardsley, R.C., Limeburner, R., 1995. Winds in the strait of Gibraltar. Q. J. R. Meteorol. Soc. 121, 1903–1921. https://doi.org/10.1002/qj.49712152807.

Draxler, R.R., Hess, G.D., 1998. An overview of the HYSPLIT_4 modelling system for trajectories, dispersion and deposition. Aust. Meteorol. Mag. 47, 295–308.

EEA, 2018. Air quality in Europe — 2018 report. EEA Report No 12/2018. European Environmental Agency, Copenhagen https://doi.org/10.2800/777411.

EEA, 2019. Air quality in Europe — 2019 report. EEA Report No 10/2019. European Environmental Agency, Copenhagen https://doi.org/10.2800/822355.

Eremenko, M., Dufour, G., Foret, G., Keim, C., Orphal, J., Beekmann, M., Bergametti, G., Flaud, J.M., 2008. Tropospheric ozone distributions over Europe during the heat wave in July 2007 observed from infrared nadir spectra recorded by IASI. Geophys. Res. Lett. 35, 1–5. https://doi.org/10.1029/2008GL034803.

Escudero, M., Lozano, A., Hierro, J., del Valle, J., Mantilla, E., 2014. Urban influence on increasing ozone concentrations in a characteristic Mediterranean agglomeration. Atmos. Environ. 99, 322–332. https://doi.org/10.1016/j.atmosenv.2014.09.061.

Escudero, M., Lozano, A., Hierro, J., Tapia, O., del Valle, J., Alastuey, A., Moreno, T., Anzano, J., Querol, X., 2016. Assessment of the variability of atmospheric pollution in National Parks of mainland Spain. Atmos. Environ. 132, 332–344. https://doi.org/10.1016/j.atmosenv.2016.03.006.

Escudero, M., Segers, A., Kranenburg, R., Querol, X., Alastuey, A., Borge, R., De La Paz, D., Gangoiti, G., Schaap, M., 2019. Analysis of summer O3 in the Madrid air basin with the LOTOS-EUROS chemical transport model. Atmos. Chem. Phys. 19, 14211–14232. https://doi.org/10.5194/acp-19-14211-2019.

European Parliament, Council of the European Union, 2008. DIRECTIVE 2008/50/EC OF THE EUROPEAN PARLIAMENT AND OF THE COUNCIL of 21 May 2008 on ambient air quality and cleaner air for Europe. Off. J. Eur. Union 44.

Fawole, O.G., Cai, X., MacKenzie, A.R., 2017. Evidence for a gas-flaring source of alkanes leading to elevated ozone in air above West Africa. African J. Environ. Sci. Technol. 11, 532–543. https://doi.org/10.5897/AJEST2016.2252.

Foret, G., Hamaoui, L., Schmechtig, C., Eremenko, M., Keim, C., Dufour, G., Boynard, A., Coman, A., Ung, A., Beekmann, M., 2009. Evaluating the potential of IASI ozone observations to constrain simulated surface ozone concentrations. Atmos. Chem. Phys. 9, 8479–8491. https://doi.org/10.5194/acp-9-8479-2009.

Fowler, A.M., Brooks, I.M., 2006. Entrainment Zone Definitions: A Large Eddy Study [WWW Document]. URL papers3://publication/uuid/FD0B57AB-382F-4236-9065-4115660CF99C.

Gangoiti, G., Alonso, L., Navazo, M., Albizuri, A., Perez-Landa, G., Matabuena, M., Valdenebro, V., Maruri, M., Antonio García, J., Millán, M.M., 2001. Regional transport of pollutants over the Bay of Biscay: analysis of an ozone episode under a blocking anticyclone in west-central Europe. Atmos. Environ. 36, 1349–1361. https://doi.org/10.1016/S1352-2310(01)00536-2.

Gangoiti, G., Alonso, L., Navazo, M., Antonio Garcia, J., Millán, M.M., 2006. North African soil dust and European pollution transport to America during the warm season:

hidden links shown by a passive tracer simulation. J. Geophys. Res. Atmos. 111, 1–25. doi:https://doi.org/10.1029/2005JD005941.

Gaudel, A., Cooper, O.R., Ancellet, G., Barret, B., Boynard, A., Burrows, J.P., Clerbaux, C., Coheur, P.F., Cuesta, J., Cuevas, E., Doniki, S., Dufour, G., Ebojie, F., Foret, G., Garcia, O., Granados-Muñoz, M.J., Hannigan, J.W., Hase, F., Hassler, B., Huang, G., Hurtmans, D., Jaffe, D., Jones, N., Kalabokas, P., Kerridge, B., Kulawik, S., Latter, B., Leblanc, T., Le Flochmoën, E., Lin, W., Liu, J., Liu, X., Mahieu, E., McClure-Begley, A., Neu, J.L., Osman, M., Palm, M., Petetin, H., Petropavlovskikh, I., Querel, R., Rahpoe, N., Rozanov, A., Schultz, M.G., Schwab, J., Siddans, R., Smale, D., Steinbacher, M., Tanimoto, H., Tarasick, D.W., Thouret, V., Thompson, A.M., Trickl, T., Weatherhead, E., Wespes, C., Worden, H.M., Vigouroux, C., Xu, X., Zeng, G., Ziemke, J., 2018. Tropospheric ozone assessment report: present-day distribution and trends of tropospheric ozone relevant to climate and global atmospheric chemistry model evaluation. Elementa 6. https://doi.org/10.1525/elementa.291.

Gesch, D.B., Verdin, K.L., Greenlee, S.K., 1999. New land surface digital elevation model covers the earth. Eos (Washington. DC). 80, 69–70. https://doi.org/10.1029/99EO00050.

Granier, C., Müller, J.-F., Brasseur, G., 2000. The impact of biomass burning on the global budget of ozone and ozone precursors. In: Innes, J.L., Beniston, M., Verstraete, M.M. (Eds.), Biomass Burning and Its Inter-Relationships With the Climate System. Springer, Dordrecht, pp. 69–85 https://doi.org/10.1007/0-306-47959-1_5.

Greenslade, J.W., Alexander, S.P., Schofield, R., Fisher, J.A., Klekociuk, A.K., 2017. Stratospheric ozone intrusion events and their impacts on tropospheric ozone in the Southern Hemisphere. Atmos. Chem. Phys. 17, 10269–10290. https://doi.org/10.5194/acp-17-10269-2017.

Harrington, J.Y., Reisin, T., Cotton, W.R., Kreidenweis, S.M., 1999. Cloud resolving simulations of Arctic stratus part II: transition-season clouds. Atmos. Res. 51, 45–75. https://doi.org/10.1016/S0169-8095(98)00098-2.

HEI, 2018. State of Global Air 2018. A Special Report on the Global Exposure to Air Pollution and Its Disease Burden. https://doi.org/10.1143/JJAP.30.720.

Helfand, H.M., Labraga, J.C., 1988. Design of a nonsingular level 2.5 second-order closure model for the prediction of atmospheric turbulence. J. Atmos. Sci. 45, 113–132. https://doi.org/10.1175/1520-0469(1989)046<1631:cooanl>2.0.co;2.

INTA, 2006a. Segundo informe a la Consejería de Medio Ambiente de la Junta de Andalucía. Análisis de las concentraciones de ozono de Córdoba y Sevilla: características de las series y análisis comparativo.

INTA, 2006b. Tercer informe a la Consejería de Medio Ambiente de la Junta de Andalucía. Evaluación de las concentraciones de ozono en el área metropolitana de Sevilla.

Jacob, D.J., 1999a. Chapter 11: oxidising power of the troposphere. Introduction to Atmospheric Chemistry, pp. 199–219 https://doi.org/10.1111/j.0954-6820.1949.tb11329.x.

Jacob, D.J., 1999b. Chapter 12. Ozone air pollution. Introd. to Atmos. Chem. 232–243.

Jaffe, D.A., Zhang, L., 2017. Meteorological anomalies lead to elevated O3 in the western U.S. in June 2015. Geophys. Res. Lett. 44, 1990–1997. https://doi.org/10.1002/2016GL072010.

Jhun, I., Coull, B.A., Zanobetti, A., Koutrakis, P., 2015. The impact of nitrogen oxides concentration decreases on ozone trends in the USA. Air Qual. Atmos. Heal. 8, 283–292. https://doi.org/10.1007/s11869-014-0279-2.

Jia, L., Xu, Y., 2014. Effects of relative humidity on ozone and secondary organic aerosol formation from the photooxidation of benzene and ethylbenzene. Aerosol Sci. Technol. 48, 1–12. https://doi.org/10.1080/02786826.2013.847269.

Kalabokas, P.D., Cammas, J.P., Thouret, V., Volz-Thomas, A., Boulanger, D., Repapis, C.C., 2013. Examination of the atmospheric conditions associated with high and low summer ozone levels in the lower troposphere over the eastern Mediterranean. Atmos. Chem. Phys. 13, 10339–10352. https://doi.org/10.5194/acp-13-10339-2013.

Kalabokas, P.D., Thouret, V., Cammas, J.P., Volz-Thomas, A., Boulanger, D., Repapis, C.C., 2015. The geographical distribution of meteorological parameters associated with high and low summer ozone levels in the lower troposphere and the boundary layer over the eastern Mediterranean (Cairo case). Tellus, Ser. B Chem. Phys. Meteorol., 6 https://doi.org/10.3402/tellusb.v67.27853.

Kalabokas, P., Hjorth, J., Foret, G., Dufour, G., Eremenko, M., Siour, G., Cuesta, J., Beekmann, M., 2017. An investigation on the origin of regional springtime ozone episodes in the western Mediterranean. Atmos. Chem. Phys. 17, 3905–3928. https://doi.org/10.5194/acp-17-3905-2017.

Kaser, L., Patton, E.G., Pfister, G.G., Weinheimer, A.J., Montzka, D.D., Flocke, F., Thompson, A.M., Stauffer, R.M., Halliday, H.S., 2017. The effect of entrainment through atmospheric boundary layer growth on observed and modeled surface ozone in the Colorado front range. J. Geophys. Res. 122, 6075–6093. https://doi.org/10.1002/2016JD026245.

Lefohn, A.S., Wernli, H., Shadwick, D., Oltmans, S.J., Shapiro, M., 2012. Quantifying the importance of stratospheric-tropospheric transport on surface ozone concentrations at high- and low-elevation monitoring sites in the United States. Atmos. Environ. 62, 646–656. https://doi.org/10.1016/j.atmosenv.2012.09.004.

Lelieveld, J., Evans, J.S., Fnais, M., Giannadaki, D., Pozzer, A., 2017. The contribution of outdoor air pollution sources to premature mortality on a global scale. Nature 525, 367–371.

Lelieveld, J., Pozzer, A., Pöschl, U., Fnais, M., Haines, A., Münzel, T., 2020. Loss of life expectancy from air pollution compared to other risk factors: a worldwide perspective. Cardiovasc. Res. 116, 1910–1917. https://doi.org/10.1093/cvr/cvaa025.

Massagué, J., Carnerero, C., Escudero, M., Baldasano, J.M., Alastuey, A., Querol, X., 2019. 2005-2017 ozone trends and potential benefits of local measures as deduced from air quality measurements in the north of the Barcelona metropolitan area. Atmos. Chem. Phys. 19 (11), 7445–7465. https://doi.org/10.5194/acp-19-7445-2019.

Mellor, G.L., Yamada, T., 1982. Development of a turbulence closure model for geophysical fluid problems. Rev. Geophys. Sp. Phys. 20, 851–875.

Millán, M.M., 2014. Extreme hydrometeorological events and climate change predictions in Europe. J. Hydrol. 518, 206–224. https://doi.org/10.1016/j.jhydrol.2013.12.041.

Millán, M.M., Salvador, R., Mantilla, E., Kallos, G., 1997. Photooxidant dynamics in the Mediterranean basin in summer: results from European research projects. J. Geophys. Res. Atmos. 102, 8811–8823. https://doi.org/10.1029/96jd03610.

Millán, M.M., José Sanz, M., Salvador, R., Mantilla, E., 2002. Atmospheric dynamics and ozone cycles related to nitrogen deposition in the western Mediterranean. Environ. Pollut. 118, 167–186. https://doi.org/10.1016/S0269-7491(01)00311-6.

Monks, S.A., Arnold, S.R., Emmons, L.K., Law, K.S., Turquety, S., Duncan, B.N., Flemming, J., Huijnen, V., Tilmes, S., Langner, J., Mao, J., Long, Y., Thomas, J.L., Steenrod, S.D., Raut, J.C., Wilson, C., Chipperfield, M.P., Diskin, G.S., Weinheimer, A., Schlager, H., Ancellet, G., 2014. Multi-model study of chemical and physical controls on transport of anthropogenic and biomass burning pollution to the Arctic. Atmos. Chem. Phys. 15, 3575–3603. https://doi.org/10.5194/acp-15-3575-2015.

Monks, P.S., Archibald, A.T., Colette, A., Cooper, O., Coyle, M., Derwent, R., Fowler, D., Granier, C., Law, K.S., Mills, G.E., Stevenson, D.S., Tarasova, O., Thouret, V., Von Schneidemesser, E., Sommariva, R., Wild, O., Williams, M.L., 2015. Tropospheric ozone and its precursors from the urban to the global scale from air quality to short-lived climate forcer. Atmos. Chem. Phys. 15, 8889–8973. https://doi.org/10.5194/acp-15-8889-2015.

Paoletti, E., De Marco, A., Beddows, D.C.S., Harrison, R.M., Manning, W.J., 2014. Ozone levels in European and USA cities are increasing more than at rural sites, while peak values are decreasing. Environ. Pollut. 192, 295–299. https://doi.org/10.1016/j.envpol.2014.04.040.

Parrish, D.D., Law, K.S., Staehelin, J., Derwent, R., Cooper, O.R., Tanimoto, H., Volz-Thomas, A., Gilge, S., Scheel, H.E., Steinbacher, M., Chan, E., 2012. Long-term changes in lower tropospheric baseline ozone concentrations at northern mid-latitudes. Atmos. Chem. Phys. 12, 11485–11504. https://doi.org/10.5194/acp-12-11485-2012.

Pay, M.T., Gangoiti, G., Guevara, M., Napelenok, S., Querol, X., Jorba, O., Pérez García-Pando, C., 2019. Ozone source apportionment during peak summer events over southwestern Europe. Atmos. Chem. Phys. 5467–5494. https://doi.org/10.5194/acp-2018-727.

Pérez, C., Sicard, M., Jorba, O., Comerón, A., Baldasano, J.M., 2004. Summertime recirculations of air pollutants over the north-eastern Iberian coast observed from systematic EARLINET lidar measurements in Barcelona. Atmos. Environ. 38, 3983–4000. https://doi.org/10.1016/j.atmosenv.2004.04.010.

Pey, J., Querol, X., De La Rosa, J., González-Castanedo, Y., Alastuey, A., Gangoiti, G., Sánchez De La Campa, A., Alados-Arboledas, L., Sorribas, M., Pio, C., Cachorro, V., Piñeiro, M., López-Mahia, P., García-Gacio, D., 2008. Characterization of a long range transport pollution episode affecting PM in SW Spain. J. Environ. Monit. 10, 1158–1171. https://doi.org/10.1039/b809001g.

Pielke, R.A., Cotton, W.R., Walko, R.L., Tremback, C.J., Lyons, W.A., Grasso, L.D., Nicholls, M.E., Moran, M.D., Wesley, D.A., Lee, T.J., Copeland, J.H., 1992. A comprehensive meterological modeling system RAMS. Meteorog. Atmos. Phys. 49, 69–91.

Querol, X., Alastuey, A., Pandolfi, M., Reche, C., Pérez, N., Minguillón, M.C., Moreno, T., Viana, M., Escudero, M., Orio, A., Pallarés, M., Reina, F., 2014. 2001-2012 trends on air quality in Spain. Sci. Total Environ. 490, 957–969. https://doi.org/10.1016/j.scitotenv.2014.05.074.

Querol, X., Alastuey, A., Reche, C., Orio, A., Pallares, M., Reina, F., Dieguez, J.J., Mantilla, E., Escudero, M., Alonso, L., Gangoiti, G., Millán, M., 2016. On the origin of the highest ozone episodes in Spain. Sci. Total Environ. 572, 379–389. https://doi.org/10.1016/j.scitotenv.2016.07.193.

Querol, X., Gangoiti, G., Mantilla, E., Alastuey, A., Minguillón, M.C., Amato, F., Reche, C., Viana, M., Moreno, T., Karanasiou, A., Rivas, I., Pérez, N., Ripoll, A., Brines, M., Ealo, M., Pandolfi, M., Lee, H.K., Eun, H.R., Park, Y.H., Escudero, M., Beddows, D., Harrison, R.M., Bertrand, A., Marchand, N., Lyasota, A., Codina, B., Olid, M., Udina, M., Jiménez-Esteve, B., Jiménez-Esteve, B.B., Alonso, L., Millán, M., Ahn, K.H., 2017. Phenomenology of high-ozone episodes in NE Spain. Atmos. Chem. Phys. 17, 2817–2838. https://doi.org/10.5194/acp-17-2817-2017.

Querol, X., Alastuey, A., Gangoiti, G., Perez, N., Lee, H.K., Eun, H.R., Park, Y., Mantilla, E., Escudero, M., Titos, G., Alonso, L., Temime-Roussel, B., Marchand, N., Moreta, J.R., Revuelta, M.A., Salvador, P., Artíñano, B., Dos Santos, S.G., Anguas, M., Notario, A., Saiz-Lopez, A., Harrison, R.M., Millán, M., Ahn, K.H., 2018. Phenomenology of summer ozone episodes over the Madrid metropolitan area, Central Spain. Atmos. Chem. Phys. 18, 6511–6533. https://doi.org/10.5194/acp-18-6511-2018.

Querol, X., Pérez, N., Reche, C., Ealo, M., Ripoll, A., Tur, J., Pandolfi, M., Pey, J., Salvador, P., Moreno, T., Alastuey, A., 2019. African dust and air quality over Spain: is it only dust that matters? Sci. Total Environ. 686, 737–752. https://doi.org/10.1016/j.scitotenv.2019.05.349.

Reynolds, R.W., Smith, T.M., Liu, C., Chelton, D.B., Casey, K.S., Schlax, M.G., 2007. Daily high-resolution-blended analyses for sea surface temperature. J. Clim. 20, 5473–5496. https://doi.org/10.1175/2007JCLI1824.1.

Richards, N.A.D., Arnold, S.R., Chipperfield, M.P., Miles, G., Rap, A., Siddans, R., Monks, S.A., Hollaway, M.J., 2013. The Mediterranean summertime ozone maximum: global emission sensitivities and radiative impacts. Atmos. Chem. Phys. 13, 2331–2345. https://doi.org/10.5194/acp-13-2331-2013.

Safieddine, S., Boynard, A., Coheur, P.F., Hurtmans, D., Pfister, G., Quennehen, B., Thomas, J.L., Raut, J.C., Law, K.S., Klimont, Z., Hadji-Lazaro, J., George, M., Clerbaux, C., 2014. Summertime tropospheric ozone assessment over the Mediterranean region using the thermal infrared IASI/MetOp sounder and the WRF-Chem model. Atmos. Chem. Phys. 14, 10119–10131. https://doi.org/10.5194/acp-14-10119-2014.

Stein, A.F., Draxler, R.R., Rolph, G.D., Stunder, B.J.B., Cohen, M.D., Ngan, F., 2015. Noaa's hysplit atmospheric transport and dispersion modeling system. Bull. Am. Meteorol. Soc. 96, 2059–2077. https://doi.org/10.1175/BAMS-D-14-00110.1.

Stevenson, D.S., Dentener, F.J., Schultz, M.G., Ellingsen, K., van Noije, T.P.C., Wild, O., Zeng, G., Amann, M., Atherton, C.S., Bell, N., Bergmann, D.J., Bey, I., Butler, T., Cofala, J., Collins, W.J., Derwent, R.G., Doherty, R.M., Drevet, J., Eskes, H.J., Fiore, A.M., Gauss, M., Hauglustaine, D.A., Horowitz, L.W., Isaksen, I.S.A., Krol, M.C., Lamarque, J.F.,

Lawrence, M.G., Montanaro, V., Müller, J.F., Pitari, G., Prather, M.J., Pyle, J.A., Rast, S., Rodriquez, J.M., Sanderson, M.G., Savage, N.H., Shindell, D.T., Strahan, S.E., Sudo, K., Szopa, S., 2006. Multimodel ensemble simulations of present-day and near-future tropospheric ozone. J. Geophys. Res. Atmos. 111. https://doi.org/10.1029/2005JD006338.

Tombrou, M., Bossioli, E., Kalogiros, J., Allan, J.D., Bacak, A., Biskos, G., Coe, H., Dandou, A., Kouvarakis, G., Mihalopoulos, N., Percival, C.J., Protonotariou, A.P., Szabó-Takács, B., 2015. Physical and chemical processes of air masses in the Aegean Sea during Etesians: Aegean-GAME airborne campaign. Sci. Total Environ. 506–507, 201–216. https://doi.org/10.1016/j.scitotenv.2014.10.098.

Tremback, C.J., Lyons, W.A., Thorson, W.P., Walko, R.L., 1994. An emergency response and local weather forecasting software system. Air Pollut. Model. Its Appl. X, 423–429 https://doi.org/10.1007/978-1-4615-1817-4_46.

Veefkind, J.P., Aben, I., McMullan, K., Föster, H., de Vries, J., Otter, G., Claas, J., Eskes, H.J., de Haan, J.F., Kleipool, Q., van Weele, M., Hasekamp, O., Hoogeveen, R., Landgraf, J., Snel, R., Tol, P., Ingmann, P., Voors, R., Kruizinga, B., Vink, R., Visser, H., Levelt, P.F., 2012. TROPOMI on the ESA Sentinel-5 precursor: a GMES mission for global observations of the atmospheric composition for climate, air quality and ozone layer applications. Remote Sens. Environ. 120, 70–87. https://doi.org/10.1016/j.rse.2011.09.027.

WHO, 2006. WHO Air Quality Guidelines for Particulate Matter, Ozone, Nitrogen Dioxide and Sulfur Dioxide: Global Update 2005: Summary of Risk Assessment. World Health Organization.

WHO, 2016. Ambient Air Pollution: A Global Assessment of Exposure and Burden of Disease. World Health Organization.

Xiong, Y., Du, K., 2020. Source-resolved attribution of ground-level ozone formation potential from VOC emissions in metropolitan Vancouver. BC. Sci. Total Environ., 721 https://doi.org/10.1016/j.scitotenv.2020.137698.

Young, P.J., Archibald, A.T., Bowman, K.W., Lamarque, J.-F., Naik, V., Stevenson, D.S., Tilmes, S., Voulgarakis, A., Wild, O., Bergmann, D., Cameron-Smith, P., Cionni, I., Collins, W.J., Dalsøren, S.B., Doherty, R.M., Eyring, V., Faluvegi, G., Horowitz, L.W., Josse, B., Lee, Y.H., MacKenzie, I.A., Nagashima, T., Plummer, D.A., Righi, M., Rumbold, S.T., Skeie, R.B., Shindell, D.T., Strode, S.A., Sudo, K., Szopa, S., Zeng, G., 2013. Pre-industrial to end 21st century projections of tropospheric ozone from the atmospheric chemistry and climate model Intercomparison project (ACCMIP). Atmos. Chem. Phys. 13, 2063–2090. https://doi.org/10.5194/acp-13-2063-2013.

Zanis, P., Hadjinicolaou, P., Pozzer, A., Tyrlis, E., Dafka, S., Mihalopoulos, N., Lelieveld, J., 2014. Summertime free-tropospheric ozone pool over the eastern Mediterranean/middle east. Atmos. Chem. Phys. 14, 115–132. https://doi.org/10.5194/acp-14-115-2014.

Zhu, L., Jacob, D.J., Mickley, L.J., Marais, E.A., Cohan, D.S., Yoshida, Y., Duncan, B.N., Abad, G.G., Chance, K.V., 2014. Anthropogenic emissions of highly reactive volatile organic compounds in eastern Texas inferred from oversampling of satellite (OMI) measurements of HCHO columns. Environ. Res. Lett. 9. https://doi.org/10.1088/1748-9326/9/11/114004.

Zong, R., Yang, X., Wen, L., Xu, C., Zhu, Y., Chen, T., Yao, L., Wang, L., Zhang, J., Yang, L., Wang, X., Shao, M., Zhu, T., Xue, L., Wang, W., 2018. Strong ozone production at a rural site in the North China Plain: mixed effects of urban plumesand biogenic emissions. J. Environ. Sci. (China) 71, 261–270. https://doi.org/10.1016/j.jes.2018.05.003.